UNIVERSITY OF CALIFORNIA
RIVERSIDE

Optical Characterization of Two Dimensional Semiconductor

A Dissertation submitted in partial satisfaction
of the requirements for the degree of

Doctor of Philosophy

in

Physics

by

Patrick Michael Odenthal

August 2015

Dissertation Committee:
Dr. Harry Tom, Committee Co-Chairperson
Dr. Roland Kawakami, Committee Co-Chairperson
Dr. Ludwig Bartels

The Dissertation of Patrick Michael Odenthal is approved:

_____

_____

Committee Co-Chairperson

_____

Committee Co-Chairperson

University of California, Riverside

ACKNOWLEDGEMENTS

I would like to thank my Advisor Dr. Roland Kawakami for always being there and making things happen. I also thank him for allowing to work in other labs during my time which gave me an opportunity to see other ways of doing research and learn many techniques that I would no have otherwise had exposure to. I would like to thank Dr. Ludwig Bartels and Dr. Scott Crooker for allowing me to come work in there labs. It was an invaluable learning experience that greatly enhanced my PhD. I also thank Dr. Harry Tom for being my local advisor once Dr. Kawakami left for The Ohio State University.

I would like to Adrian Swartz and Jared Wong for taking the time to train me. Most of my lab skills stem from you and have served me well in my time here. I also thank Kathy McCreary and Wei Han for putting up with my questions when Adrian and Jared weren't around.

I would like to thank Igor Pinchuk for his work on developing germanane. Without his work most of this thesis would no have been possible.

I would like to thank team Riverside, Walid Amamou and Dante O'hara. They stayed behind with me when most of the lab moved to Ohio. Also there work was instrumental in me getting my first paper.

I would also like to thank all of the lab members of the Kawakami, Bartels and Crooker groups for there help and the good times that we shared in the lab.

Finally I would like to thank my new wife Lacey for constantly supporting me and being there for me. Without you I would never have made it through my PhD.

ABSTRACT OF THE DISSERTATION

Optical Characterization of Two Dimensional Semiconductor

by

Patrick Michael Odenthal

Doctor of Philosophy, Graduate Program in Physics
University of California, Riverside, August 2015
Dr. Harry Tom, Chairperson

The world is silicon based technology is about to come to a close as it rapidly approaches the quantum limit. New materials are required for further technological advances. The optical properties of two of these new materials, germanane (GeH) and molybdenum disulfide (MoS_2) are studied in this thesis.

Germanane is synthesized using MBE co-deposition, resulting in atomic control of thickness with wafer scale size. Unfortunately, germanane is grown on germanium substrates which are conductive and opaque to light near the band edge. We have developed a large area transfer method using electrochemical delimitation (ie. Bubble transfer) to arbitrary substrates. Germanane films with thickness ranging from 1 nm to 600 nm and areas up to $\sim$1 cm^2 have been reliably transferred. Characterization by photoluminescence, x-ray diffraction, and energy-dispersive X-ray spectroscopy in-

dicate that the films quality is preserved after transfer. The optical and electro-optical properties of germanane can now be measured. Temperature dependent photoluminescence excitation spectroscopy (PLE), absorption and photo conductivity show a band edge near 1.9 eV with a large Urbach tail. Photoluminescence (PL) measurements show a broad luminescence that is shifted by 700 meV from the absorption edge. We also observe an increase of the PL intensity of several orders of magnitude from room temperature to 4 K. Time resolved photoluminescence (TRPL) reveal many time scales ranging from a few ns to a s.

Sputtering of MoS_2 films of single-layer thickness by low-energy argon ions selectively reduces the sulfur content of the material without significant depletion of molybdenum. X-ray photoelectron spectroscopy shows little modification of the Mo 3d states during this process, suggesting the absence of significant reorganization or damage to the overall structure of the MoS_2 film. Accompanying *ab initio* molecular dynamics simulations find clusters of sulfur vacancies in the top plane of single-layer MoS_2 to be structurally stable. Measurements of the photoluminescence at temperatures between 175 and 300 K show quenching of almost 80% for an 10% decrease in sulfur content.

Contents

List of Tables **xiii**

List of Figures **xiv**

1 Two Dimensional Materials **1**

1.1 Introduction 1

1.2 Germanane 2

1.3 Molybdenum Disulfide 4

2 Experimental Techniques **6**

2.1 Introduction 6

2.2 Molecular Beam Epitaxy 7

2.3 Photoluminescence 8

2.3.1 Theory 8

2.3.2 Setup 10

2.4 Absorption 12

2.4.1 Theory 12
2.4.2 Setup 13
2.5 Photoluminescence Excitation Spectroscopy 14
2.5.1 Theory 14
2.5.2 Setup 14
2.6 Time Resolved Photoluminescence 15
2.6.1 Theory 15
2.6.2 Setup 15

3 Synthesis of germanane **17**
3.1 Introduction 17
3.2 MBE growth of $CaGe_2$ by co-deposition 19
3.3 Comparison of $CaGe_2$ grown by other methods 24
3.4 Conversion of $CaGe_2$ to Germanane 26
3.5 Air stability of $CaGe_2$ 29
3.6 Characterization of germanane grown by Co-deposition 30
3.7 Conclusion 34

4 Large Area Germanane on Arbitrary Substrates **35**
4.1 Introduction 35
4.2 Large Area Transfer 37
4.3 Characterization of transfered germanane 40

4.4 Electron transport and photoconductivity 42

4.5 Conclusion 46

5 Optical Properties of Germanane **48**

5.1 Introduction 48

5.2 Photoluminescence 49

5.3 Photoluminescence excitation spectroscopy 51

5.4 Absorption 52

5.5 Wavelength dependent photo-conductivity 54

5.6 Time correlated single photo counting 56

5.7 Conclusion 58

6 Controlled argon beam-induced desulfurization of monolayer molyb- denum disulfide **59**

6.1 Introduction 60

6.2 Methods 60

6.3 Results and Discussion 63

6.4 Conclusion 70

7 Conclusion **71**

Bibliography **73**

A Optics Tricks **81**

A.1 Introduction 81
A.2 F-number and Numerical Aperture 81
A.3 White light sources 83
A.4 Dealing with fiber optics 84
A.5 Coupling into a spectrometer 86
A.6 Correcting a photoluminescence spectrum using white light 88

B Photoluminescence Alignment **90**

B.1 Introduction 90
B.1.1 Setup 90
B.2 Setup 91
B.2.1 Light source and sample holder selection 91
B.2.2 Laser 92
B.2.3 Beam splitter and sample holder 94
B.2.4 Focus and collection lens 95
B.2.5 Coupling to a spectrometer 97
B.3 Optimizing signal 98
B.3.1 Troubleshooting 99

C Scanning Laser Microscope **100**

C.1 Introduction 100
C.2 Design 101

C.3 Alignment Instructions 102
C.3.1 Aligning the first stage 103
C.3.2 Aligning the second stage 103
C.3.3 Aligning the third stage 103
C.4 Characterization of Performance 104

List of Tables

3.1 Elemental composition of germanane films for various de-intecalation times 29

4.1 Elemental composition of germanane films by EDS 42

List of Figures

1.1 Structure and band structure of germanane 2

1.2 Structure and band structure of MoS_2 4

2.1 Diagram of an MBE chamber 7

2.2 How Photoluminescence works 8

2.3 Photoluminescence setups 10

2.4 A typical absorption curve 12

2.5 Absorption Setup 13

2.6 Photoluminescence Excitation Spectroscopy Setup 14

2.7 Time resolved single photon counting setup 15

3.1 RHEED images at several stages in the GeH growth process 20

3.2 RHEED of GeH grown at various temperatures 23

3.3 RHEED of GeH grown by different methods 26

3.4 Photoluminescence of Geh de-intercalated for several different times . 27

3.5 $CaGe_2$ oxidation 30

3.6 Characterization of GeH grown by co-deposition 31

3.7 GeH morphology 32

4.1 Schematic and photos of germanane transfer 37

4.2 Micrographs of Transfered Germanane 39

4.3 XRD and Photoluminescence of Germanane before and after transfer . 41

4.4 Intensity dependence of Germanane's photocurrent 43

4.5 Wavelength dependence of Germanane's photocurrent 44

5.1 Temperature and power dependent PL of Germanane 49

5.2 PLE of Germanane 51

5.3 Absorbance of Germanane 53

5.4 Wavelength dependent photo conductivity 55

5.5 Time correlated single photon counting 57

6.1 Model of sputtered $MoS2$ 61

6.2 XPS analysis of sputtered $MoS2$ 64

6.3 Photoluminescence of sputtered $MoS2$ 68

A.1 Diagram of a Lens 82

A.2 Collimating a non point source 83

A.3 Proper Fiber coupling 84

A.4 How a Czerny-Turner spectrometer works 87

A.5 How to correct a PL spectrum using white light 89

B.1 Picture of a PL setup 90

B.2 PL laser setup 92

B.3 setup of the beam splitter and sample holder 94

B.4 setup of the focus and collection lens 96

B.5 Fiber Coupling to the spectrometer 97

C.1 Images of the Scanning Laser Microscope 101

C.2 Characterization of the Scanning Laser Microscope 105

Chapter 1

Two Dimensional Materials

1.1 Introduction

The main drive behind my research is the push for smaller, faster and more efficient electronics. Traditional silicon based electronics have made gains in speed and efficiency by shrinking there feature size. This is about to run into the quantum limit. The fundamental principles of how electronics work will have to radically change to increase the performance of electronics beyond the quantum limit. One idea is to use the electron's spin degree of freedom to transport and store information. This are a research is called spintronics. In order for the dream of spintronics to be realized we must discover materials that have long spin coherence lifetimes and long spin diffusions lengths [5]. One promising class of materials are the two dimensional (2D) materials.

The preeminent example of the 2D materials is graphene which was first isolated by Novoselov and Geim in 2004 [51]. Graphene has many novel properties such as gate tunable Fermi level, extreme sensitivity to surface dopants [46, 47, 57] and quantum Hall effect [86]. Recently there has been intense interest in 2D materials beyond graphene that have a native band gap and stronger spin-orbit coupling [8, 35, 42, 61]. Two of these new materials, germanane (GeH) and molybdenum disulfide (MoS_2), are studied in this thesis. A brief description of each and a summary of there important properties are given below.

1.2 Germanane

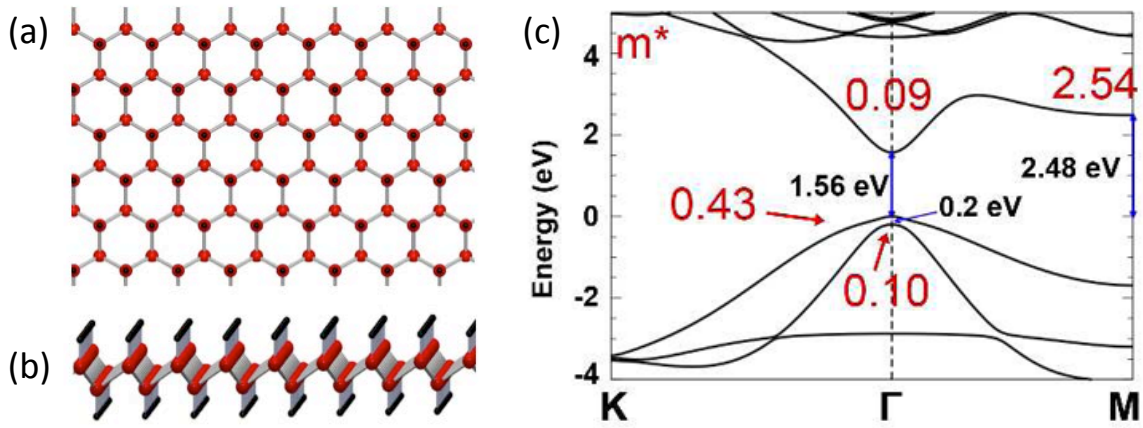

Figure 1.1: (a) Top view of GeH (b) side view of GeH (c) band structure of GeH adapted from [8]

Germanane is the germanium analogy of graphane, hydrogen terminated graphene. It is a buckled honeycomb of germanium that is stabilized by one hydrogen per germanium atom as seen in Figure 1.1a and b. Like graphene it has direct bandgap

at the Γ-point (Figure 1.1c) that can be tuned via surface covalent functionalization [8, 23, 63]. Additionally, germanane is air stable and has a high predicted mobility of 18,000 $\frac{cm^2}{Vs}$ at room temperature, making it extremely promising for electronic and optoelectronic applications. [8, 63] Specifically, the combination of high mobility, non-zero bandgap, and low dimensionality are advantageous for short channel field effect transistors (FETs) with high on-off ratios and low quiescent currents [61]. Furthermore, germananes large spin orbit coupling makes it possible to explore novel physical phenomena such as quantum spin Hall effect at room temperature [39, 64, 81].

One of the biggest challenges to realizing germanane's exciting properties is the creating of single layer material. Bianco *et al* [8] successfully isolated single layer germanane from bulk crystals using micro-mechanical ex-foliation. These flakes were small and difficult to produce. A much more robust way to synthesize germanane is needed. Chapter 3 describes a method to produce large area thin germanane by molecular beam epitaxy (MBE) that is hoped to soon be extended to single layer germanane. The MBE growth brings another set of problems. The required growth substrate is conductive and opaque to light near the bandgap. Chapter 4 describes a transfer process that eliminates these problems. Finally, before any novel phenomena can be explored the basic properties such as bandgap energy and carrier lifetime must be determined. Chapter 5 explores these properties optically.

1.3 Molybdenum Disulfide

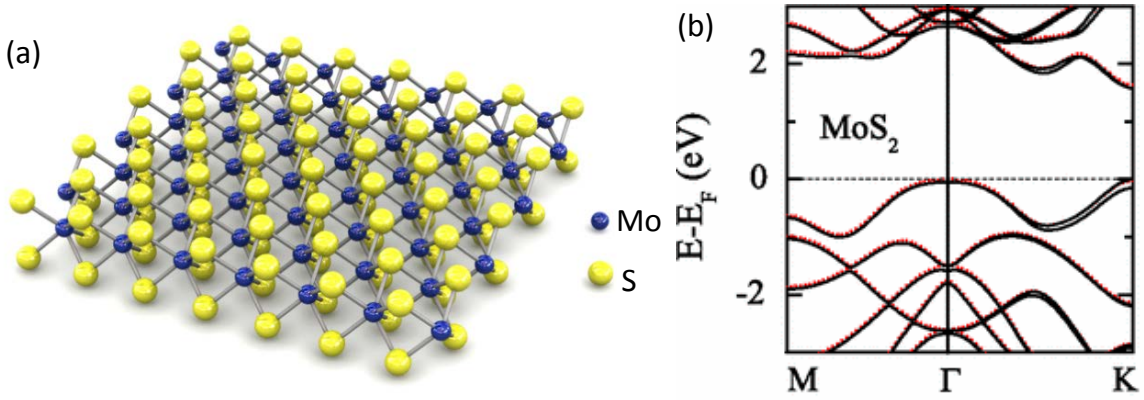

Figure 1.2: (a) structure of MoS_2 adapted from [6] (c) band structure of MoS_2 adapted from [87]

MoS_2 consist of a trilayer of sulfur-molybdenum-sulfur (Figure xxx) and has a very interesting electronic structure. Bulk MoS_2 has a indirect bandgap at 1.4 eV that transitions to a direct bandgap of 1.9 eV at the K-point in the monolayer limit (Figure 1.2) [42, 66]. The conduction band has a spin splitting at the K-point of 150 meV leading to predictions of long spin lifetimes [41, 87]. In addition to this interesting electronic structure, MoS_2 has many established applications in catalysis, such as for hydrodesulfurization [7, 26], and it recently received attention as an electrode material for water splitting [25, 32].

Single-layer MoS_2 field effect transistors (FET) have been fabricated with mobilities on the order of 1 $\frac{cm^2}{Vs}$ and higher [15, 30, 36, 61], as well as on-off ratios up to 10^8 at room temperature. Bulk MoS_2, and most mono- or few-layer MoS_2 materials examined to date, exhibit n-doping [15, 30, 36, 61], but p-doping has also been

observed [83]. Ambipolar operation has been achieved by gating with an ionic liquid [85]. Another distinctive electronic property is the possibility of selective valley population of the monolayer, which has been achieved using excitation by circularly polarized light [10, 38, 41, 80, 82].

With any material the role of defects and modification of materials properties are important topics to understand. Chapter 6 discusses the removal of sulfur in MoS_2 by low energy argon sputtering. This enabled us to study how defects affect photoluminescence as well as activates MoS_2 for easier functionalization.

Chapter 2

Experimental Techniques

2.1 Introduction

Many techniques were used in this thesis and must be understood to fully understand the research presented. Many of the samples were grown by molecular beam epitaxy, which is an ultra high vacuum (UHV) materials deposition method. As MBE has been extensively documented in other theses from the Kawakami Lab [68, 79], only a brief description will be given here. Most of the optical techniques used in this thesis had not been previously used in the Kawakami Lab. A discussion of these techniques as well as a description of there setup will be given.

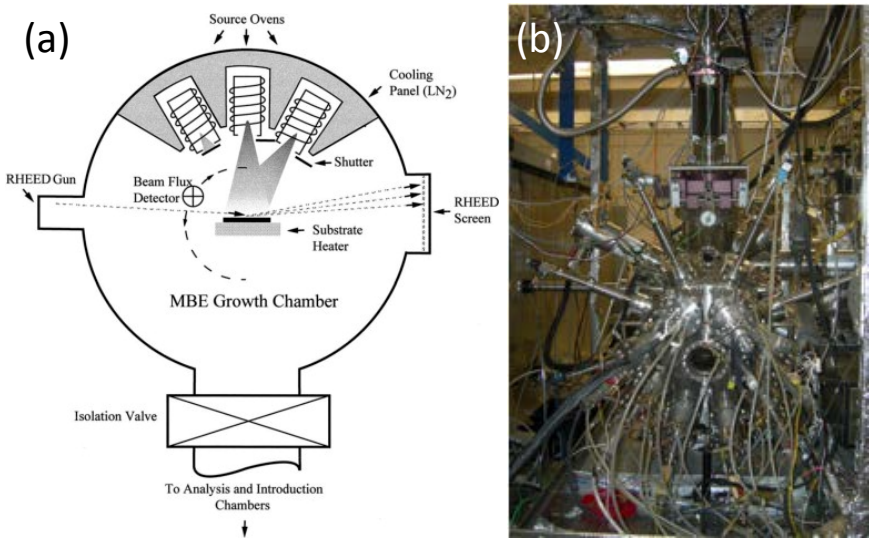

Figure 2.1: (a) Diagram of a MBE chamber adapted from [3]. (b) A picture of one of the Kawakami lab MBE chambers

2.2 Molecular Beam Epitaxy

MBE was invented in the late 1960s by A. Cho and J. Aurther [12, 45]. There technique uses UHV and element evaporation sources to gain atomic level control of materials growth. MBE is kind of like spray paint except evaporated elements are used instead of paint and kinetic energy from the evaporation is used instead of a carrier gas. Also like painting, MBE can only build upon a starting substrate and can't created a sample from nothing. In MBE elemental sources are evaporated, forming molecular beams. UHV significantly lowers the evaporation temperature allowing for the evaporation of many elements using a simple resistive heater. The molecular beams spread radially until they strike the sample or chamnber wall where they condense. The transport of material by molecular beams is made possible by the long mean free paths in the UHV environment. If there is a lattice match with the starting

substrate the deposited material will follow the pattern and also be crystalline. More complex materials can be formed by flux matching multiple source materials or using distillation to ensure stoichiometry [3, 12, 19].

2.3 Photoluminescence

2.3.1 Theory

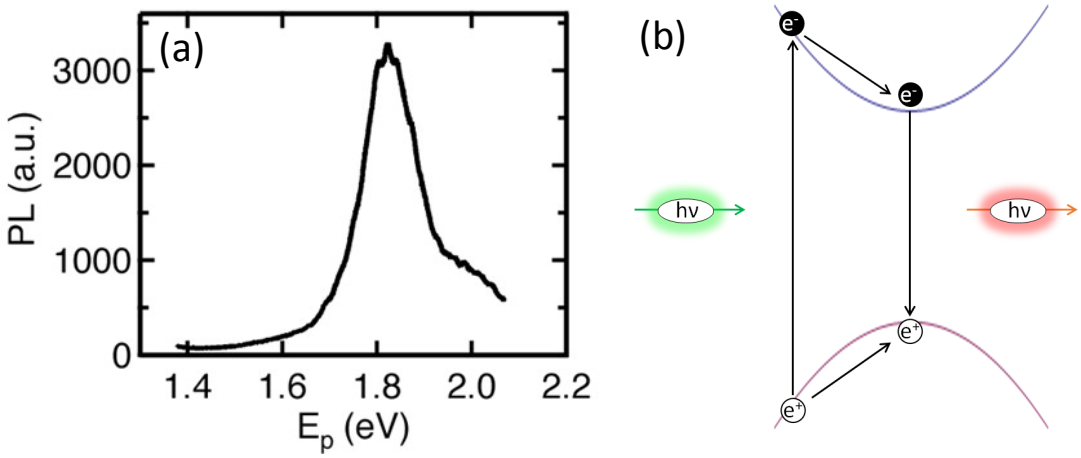

Figure 2.2: (a) PL spectrum of MoS_2 showing the typical shape. (b) a pictorial representation of the mechanics behind PL

Photoluminescence (PL) is a technique use to study the band gap of direct gap semiconductors where light is emitted from the recombination of photo-excited electrons. How PL works for direct gap semiconductors is described below. First an electron from the conduction band is photo-excited using light that is above the band gap energy. The excited electron the relax to the bottom of the valence band through no radiative processes. At the same time, the photo generated hole floats to the top

of the conduction band. The electron hole pair then recombines producing and photon [34, 54, 62]. Figure 2.2 shows a schematic of the entire process and a typical spectrum.

In the simplest case the photon is emitted at the bandgap energy. There are a couple things that can make this not true. In some semiconductors, e.g. MoS_2 and WSe_2, the electron and hole can form a bound state called an exciton [54]. This bound states decreases the energy of the electron hole pair red shifting the photon luminescence. This shifting can be quite large. In WSe_2 the binding energy is 0.37 eV which is a significant percentage of the band gap, 2.02 eV [18]. In two dimensional materials, the bound state can become charge absorbing another hole or electron forming a trion further reducing the energy [40]. Defects can also shift the PL away from the band edge. In this case the PL comes from a sub bandgap defect state [62].

Many changes can be seen in the PL spectrum as temperature is changes. First, as temperature is increased the PL center red-shifts. This is expected as the bandgap decreases with temperature in a typical semiconductor [72]. It is common for PL to broaden with increasing temperature. The extra energy for the increased temperature allows the electrons and holes to move around which moves the energies at which the electrons and holes are at before recombination. Finally, PL intensity can decrease with increasing temperature. The mechanisms for this can very and are not discussed here.

2.3.2 Setup

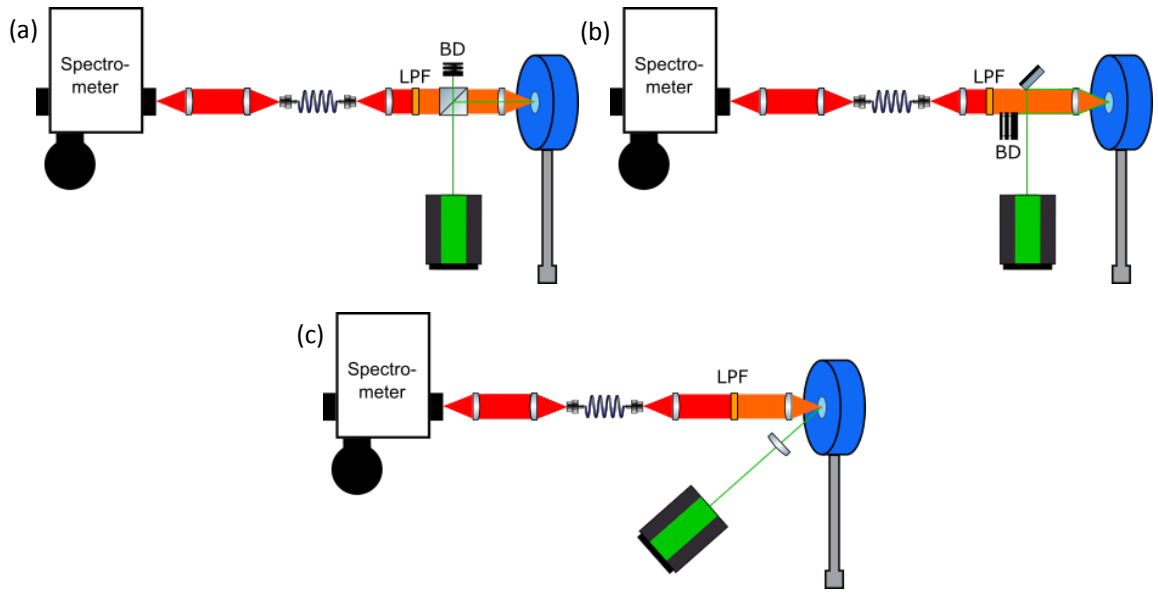

Figure 2.3: The three different setups used for PL. LPF stands for long pass filter and BD stands for beam dump.

Several different setups for photoluminescence were used in this thesis. Each has advantages and disadvantages. None were found to be significantly better then the others. Each setup will described as well as there advantages and disadvantages.

The PL setup in Figure 2.3a is the easiest and works for applications with large signal size. Start with a collimated monochromatic light source, typically a laser, and use a beam splitter or dichroic mirror to reflect the light 90° to where you sample is. Use a high numerical aperture (NA) lens, to focus the beam to the sample. This lens also collects and collimates the PL. The PL travels back through beam splitter where the excitation light is removed by a long pass filter (LPF) and the remaining light is coupled into a spectrometer. This can be done using a fiber as shown in Figure 2.3a

or directly coupled. A discussion of coupling into spectrometer is given in appendix A. The biggest advantage of this setup is that the PL is collinear with the excitation light allowing the bright excitation light to be used for alignment. Also, in this setup it is very easy to replace the collection lens with a microscope objective for micro PL. To make the PL and excitation collinear one must use a beam splitter or dichroic mirror which induces loss in signal which is the biggest disadvantage of this setup. As this was the most common setup I used a extended discussion of the alignment procedure is given in appendix B.

The PL setup in Figure 2.3b is similar to the first setup but removes the beam splitter. A mirror is used to reflect the excitation light the side of the focusing/collection lens. The reflected excitation light is blocked using a beam dump (BD). Any scatter excitation is removed from the PL using a LPF before being coupled to a spectrometer. This setup has less loss then the first setup but as the PL is not collinear with the excitation light it is much harder to align the optics that couple the spectrometer. A extremely bright sample such as ZnSe quantum dots can be helpful for alignment.

The PL setup in Figure 2.3c is the most different from the first. Here the excitation light is focused to sample and a separate lens collects the PL. The scattered excitation light is again removed using a LPF before the PL is coupled to the spectrometer. In this setup there is nothing in the path of the PL to block it from the spectrometer giving it low loss in that region. The biggest disadvantaged is that the use of two

lenses limits the size of the collection lens reducing the collection efficacy. Again the Pl is not collinear with the excitation making alignment difficult.

2.4 Absorption

2.4.1 Theory

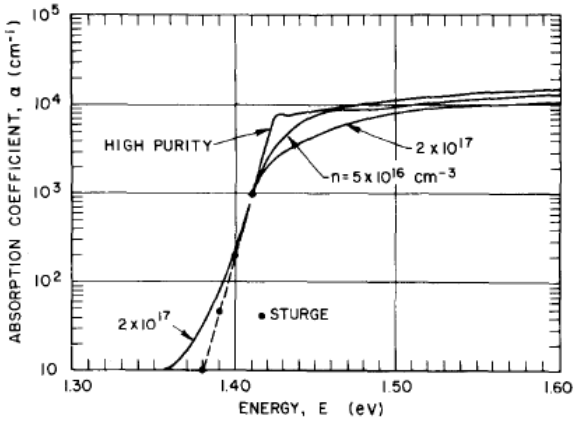

Figure 2.4: Absorption coefficient for lightly doped n-type GaAs at 297 K. Adapted from Reference [11]

Direct gap semiconductors absorb light with energy above the band edge and transmit light with energy below the band edge. The onset of strong absorption can then be a useful tool to determine the band edge [88]. Figure 2.4 shows a representative absorption curve the direct gap semiconductor GaAs. The high purity sample shows a sharp transition near the bandgap. As the amount of impurities is increased the transition broadens forming an Urbach tail [11,24]. In this case a fitting procedure described in Chapter 5 must be used to estimate the bandgap.

2.4.2 Setup

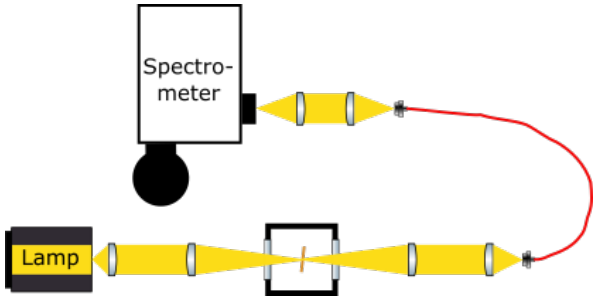

Figure 2.5: The typical absorption setup

The setup for absorption is fairly simple as seen in Figure 2.5. It is a collimated white light source that is focused through the sample and then coupled to a spectrometer. The main trick is to use achromatic optics. A more detailed discussion about dealing with white light is given in Appendix A. The mass absorption coefficient (α) can be calculated using the Beer-Lambert law, $I = I_0 e^{-\alpha d}$, where I_0 is the incident spectrum, I is the transmitted spectrum and d is the film thickness [88]. This also normalizes the data and removes any artifacts from the light source.

A more sensitive setup can be made replacing the white light with a tunable source and the spectrometer with a avalanche photo diode. In this setup up you must sweep through all the colors and measure the intensity instead of doing the entire spectrum in one go.

2.5 Photoluminescence Excitation Spectroscopy

2.5.1 Theory

Photoluminescence Excitation Spectroscopy (PLE) works by sweeping the PL excition enegry and measuring the resulting PL. PL is only emitted if the excitation is above the bandgap energy. PLE gives similar information as absorption but uses the emitted PL instead of the transmitted light. This makes it useful for samples that are not transparent [56].

2.5.2 Setup

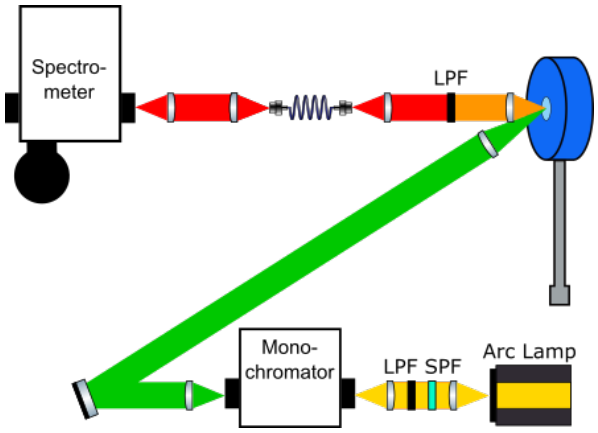

Figure 2.6: The typical PLE setup

The setup for PLE is very similar to that of PL. The only difference is that you use a tunable excitation source and achromatic optics. I created a tunable light source using an xenon arch lamp coupled through a mono-chronometer. Long pass and short pass filters were placed before the mono-chronometer to prevent overlapping

of orders from the diffraction grating. Figure 2.6 shows a typical setup using the PL setup shown in Figure 2.6c. Any of the PL setups should in principle work for PLE.

2.6 Time Resolved Photoluminescence

2.6.1 Theory

Time resolved photoluminescence (TRPL) measures the carrier lifetime. Knowledge of carrier lifetime is important bipolar transistors, laser gain medium and solar cells.TRPL was performed using time correlated single photon counting (TCSPC). PL is generated using a pulsed excitation and the time between the excitation and the first emitted photon is measured. This is done many times building a histogram. If the decay is exponential the histogram can be fit using an exponential and the time constant can be determined [76].

2.6.2 Setup

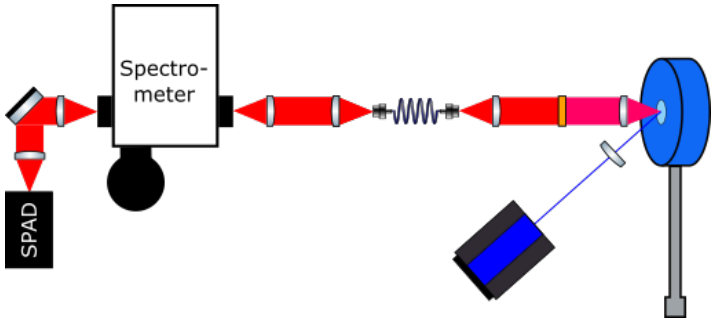

Figure 2.7: The typical TCSPC setup

As you can imagine TCSPC setup is a modified PL setup. The excitation source is replaced with a pulsed laser and the detector must be a fast single photon counting module such as a multi channel plate photomultiplier or a single photon avalanche photo diode (SPAD). A time correlated single photon counting module is hooked to the pulsed laser and detector to gain time resolution. It can be useful to place monochromator before the detector to measure carrier lifetime at different photon energies.

Chapter 3

Synthesis of germanane

Parts of this chapter were adapted from reference [58]. This was a collaborative work with many of the Kawakami group students participating. Specifically Igor Pinchuck developed the $CaGe_2$ growth recipe. The GeH conversion process and characterization presented in this chapter were performed by Walid Amamou and myself.

3.1 Introduction

An important challenge is the growth of large area, single-crystalline germanane films. The most successful effort to date has been the synthesis of $CaGe_2$ films by depositing Ca films on Ge(111) and then performing an in situ postannealing [13, 48]. The $CaGe_2$ films were then converted to germanane via HCl de-intercalation [8, 73]. While this provides an important baseline, a much stronger approach would be to perform molecular beam epitaxy (MBE) growth of $CaGe_2$ films by co-depositing Ca

and Ge atoms. This would provide much greater control over the film thickness than the postannealing method and may lead to higher quality films. Further, the MBE co-deposition approach could lead to vertically-stacked heterostructures of germanane, silicane (SiH), and their alloys through the growth of $CaGe_2CaSi_2$ heterostructures and subsequent HCl de-intercalation. However, to our knowledge, the co-deposition growth of $CaGe_2$ or $CaSi_2$ has not yet been demonstrated. We report the successful co-deposition growth of $CaGe_2$ films on Ge(111) substrates by MBE. We find that the surface structure of co-deposited $CaGe_2$ films is better than films prepared by postannealing, based on a comparison of in situ reflection high energy electron diffraction (RHEED) patterns. Furthermore, we investigate the effect of growth temperature and find the best RHEED patterns at 750 °C. Finally, the $CaGe_2$ films are immersed in HCl to de-intercalate the Ca atoms, and characterization by x-ray diffraction and Fourier transform infrared spectroscopy (FTIR) show that the resulting films are indeed germanane. *Ex situ* atomic force microscopy (AFM) indicates that the grain size is on the order of a few micrometers, being limited primarily by terraces induced by the Ge substrate. With optimization of the substrate, it may be possible to realize the long-term goal of large area germanane. These results signal a major advance for 2D semiconductors and layered van der Waals heterostructures for novel electronic, optical, and spintronic devices.

3.2 MBE growth of $CaGe_2$ by co-deposition

MBE growth is performed in an ultrahigh vacuum (UHV) chamber with base pressure of 2×10^{-10} Torr. Elemental Ge and Ca are evaporated from thermal effusion cells with high purity Ge (99.9999%, Alfa Aesar) and Ca (99.99%, Sigma Aldrich) source materials. Growth rates are determined by a quartz deposition monitor. All films are grown on undoped Ge(111) single-sided polished wafers with an average wafer thickness of 0.35 mm and an orientation tolerance of 0.5 (University Wafer). The starting 20 diameter wafer is cleaved into smaller pieces, which then undergo chemical etching to remove surface oxides/metals and replace them with a thin protective oxide film. Etching involves a sequence of steps beginning with submersion into a 10:1 mixture of H_2O:NH_4OH for 60 s followed by 60 s in a 10:1 mixture of H_2O:H_2SO_4. Finally, substrates are put into a H_2O_2 solution for 60 s before being rinsed by de-ionized (DI) water and inserted into the UHV chamber. The substrate is annealed at 650 °C for 30 min as measured by a thermocouple located near the substrate. In situ RHEED is used to monitor the sample surface throughout the growth and annealing process. The RHEED beam voltage is 15 kV unless otherwise noted. Annealing thermally desorbs the protective oxide from the Ge(111) surface. With the substrate still at 650 °C, a 5 nm Ge buffer layer is depositedwith typical rates of; 2Å/min as measured by a quartz microbalance deposition monitor. This procedure is followed for all CaGe2 films grown in this study.

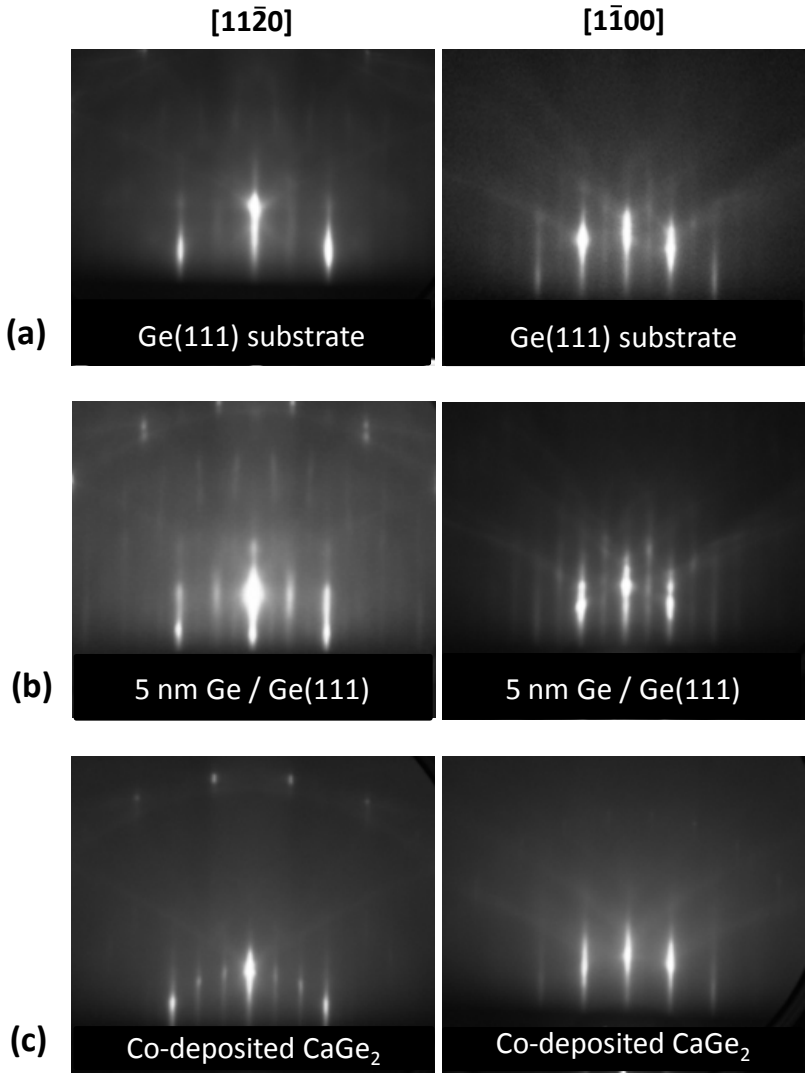

Figure 3.1: (a) RHEED patterns for a Ge(111) substrate after UHV annealing. Left and right patterns are for the 11$\bar{2}$0 and 1$\bar{1}$00 azimuths, respectively. (b) RHEED patterns after the growth of a 5 nm Ge buffer layer. (c) RHEED patterns after the growth of CaGe2 at 750 °C.

The co-deposition growth of CaGe2 films on Ge(111) is illustrated by the RHEED patterns in Figure 3.1. Figure 3.1a shows RHEED patterns of a Ge(111) surface with beam along the [11$\bar{2}$0] and [1$\bar{1}$00] in-plane directions (left and right images, respectively) after thermal annealing to remove the surface oxide. Figure 3.1b shows respective patterns after the deposition of the 5 nm Ge buffer layer. The important feature here is sharpening of the RHEED diffrac- tion streaks, indicating a flat and ordered Ge surface. In addition, the appearance of $\frac{1}{4}$ and $\frac{1}{8}$ order diffraction peaks in the [11$\bar{2}$0] direction indicates the well-established Ge 2$\times$8 reconstruction of a high quality,clean surface [21, 22, 53].

The strategy for co-deposition growth of $CaGe_2$ is to try to achieve the adsorption-limited growth regime, similar to the MBE growth of GaAs, EuO, Bi2Se3, and other materials [17, 49, 67, 70, 84]. In such growths, one of the elements is supplied at overpressure and any excess will re-evaporate from the surface (volatile species) so that the growth rate is determined by deposition of the other element (stable species). If such a growth window exists, then good stoichiometry is obtained. For example, in GaAs growth, the As (volatile species) is supplied at overpressure and the growth rate of GaAs is determined by the deposition of Ga (stable species). For the case of CaGe2, the evaporation temperature of Ge is; 1100 °C and of Ca is; 500 °C (based on typical effusion cell temperatures). Therefore, Ca may act as the volatile, re-evaporating species. Further-more, the bulk phase diagram for CaGe alloys indicates

that the $CaGe_2$ phase is stable for temperatures below; 800 °C [52]. Thus, there is the possibility for an adsorption- limited growth window between 500 and 800 °C.

For the adsorption-limited growth, the sample temperature is raised to 750 °C and the Ca and Ge fluxes are 8.1×10^{12} and $1.2 \times 10^{1}3$ $\frac{atoms}{cm^2 \cdot s}$, respectively. The flux ratio of Ca:Ge is 0.68, which has a higher Ca flux than the stoichiometric ratio of 0.5 for CaGe2 to provide the required excess Ca for adsorption-limited growth.

Here, we operationally define the growth rate of the $CaGe_2$ film as the rate determined by the Ge flux. The Ge shutter is opened first, with the Ca shutter opening 5 s later. Approximately 10 s after the opening of the Ca shutter, the RHEED pattern shows a sequence of rapid changes in the surface reconstruction until the stable patterns shown in Figure 3.1c are achieved after another 20 s. This pattern exhibits a 1×3 reconstruction, which remains for the duration of the $CaGe_2$ co-deposition (for thicknesses at least as high as 600 nm). As we verify later, this is the RHEED pattern for CaGe2. Some important features need to be highlighted here. As the Ge(111) pattern changes into the $CaGe_2$ pattern, the integer order diffraction peaks remain strongly visible (in both directions). This shows that the main structure of the surface remains unchanged, as expected for the transition from Ge(111) to the $CaGe_2$ structure. As Ca is introduced into the bulk Ge lattice, the Ge(111) planes maintain their overall structure but every two Ge planes are separated by a Ca layer. We can visualize the process by examining Figs. 1(b) and 1(c), which show projected views of Ge(111) and $CaGe_2$. For both materials, the Ge layers have the same structure. The

difference is that the $CaGe_2$ has an atomic layer of intercalated Ca to separate the individual Ge layers (two flat Ge planes can be considered as a single buckled Ge layer with honeycomb structure). The overall structure of the Ge(111) surface should stay unchanged, as shown by integer order diffraction peaks maintaining their position and intensity throughout the deposition. Thus, the evolution of the RHEED pattern is consistent with the transition from Ge(111) to CaGe2.

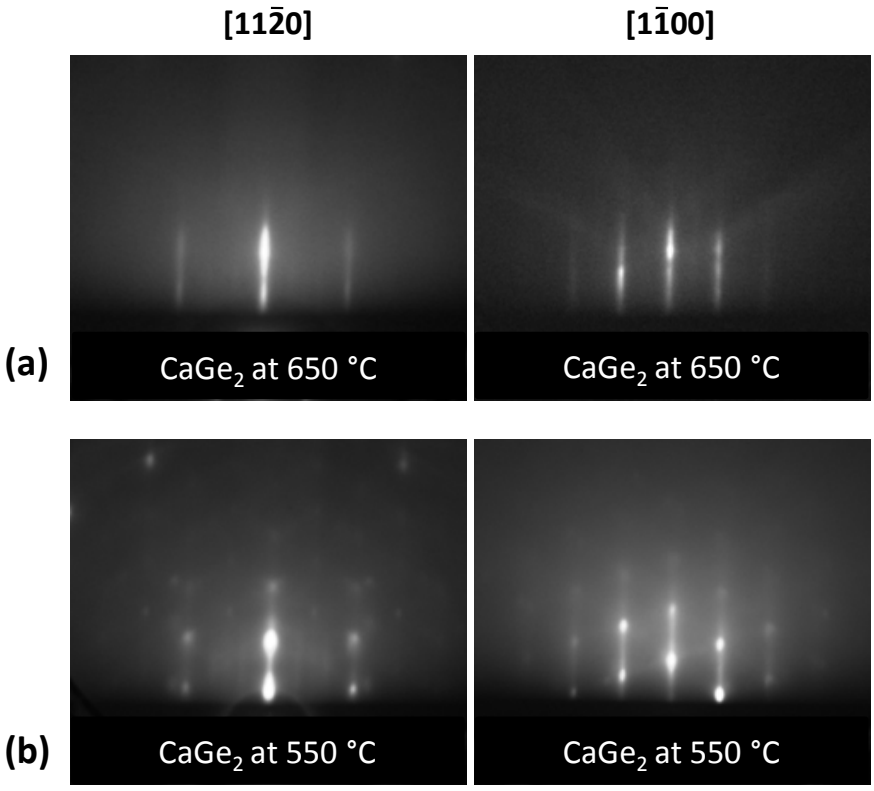

Figure 3.2: (a) RHEED patterns for co-deposited $CaGe_2$ grown at 650 °C. (b) RHEED patterns for co-deposited $CaGe_2$ grown at 550 °C.

Next, we investigate the growth temperature window by performing co-deposition growth at substrate temperatures of 650 and 550 °C. Figure 3.2a shows the RHEED patterns for 650 °C, while Figure 3.2b shows RHEED patterns for 550 °C. It is clear

that as the growth temperature is decreased, the resulting $CaGe_2$ film degrades in quality, as seen from the RHEED pattern losing the 1×3 reconstruction and the integer order streaks starting to exhibit superimposed dots. The dot pattern is indicative of a 3D reciprocal lattice, which emerges as the surface becomes slightly rougher and the RHEED beam diffracts via transmission through islands on the surface. The asymmetry of the dot pattern is due to a slight out-of-plane tilt of the sample holder.

3.3 Comparison of $CaGe_2$ grown by other methods

Previously, thin films of $CaGe_2$ by a couple of different methods which we reproduced to compare the quality of our co-deposited films. One method involves annealing a film of Ca on a Ge substrate while the other has Ca deposited onto a hot Ge substrate [13, 48, 73].

We first synthesized $CaGe_2$ using the established method of Ca deposition on Ge(111) followed by postannealing [48]. We will refer to this as the Morar growth. Starting with the annealed Ge(111) surface and growing a buffer layer of Ge, we then deposit 20 nm Ca at room temperature. During Ca growth, the RHEED pattern quickly loses its streaks and becomes featureless, indicating an amorphous Ca layer. We then proceed to heat up the sample to 750 °C to anneal and evaporate extra Ca from the surface. As the sample temperature rises, the amorphous RHEED begins to show integer order diffraction peaks of the Ge(111) lattice around 480 °C. As the

temperature continues rising, the 1×3 reconstruction peaks appear at around 690 °C and remain for the duration of the annealing process. The final RHEED pattern for post annealed $CaGe_2$ is shown in Figure 3.3a. We can see that both directions show the similar 14×3 reconstructed RHEED patterns as our co-deposition growth, so we verify that our co-deposition growth produces $CaGe_2$ films. Another important conclusion is that the RHEED pattern for the co-deposition growth is significantly better than for the postannealing growth evident from the latter showing slight polycrystalline rings in the pattern. This might be due to the formation of other stable phases such as CaGe in the postannealing method, which are suppressed in the adsorption-limited growth regime.

We next grow $CaGe_2$ using the method of depositing Ca onto a hot substrate [13, 73]. This will be referred to as the Vogg growth. We first annealed the Ge substrate and grew a 5nm Ge buffer layer. We then heat the Ge to 750 °C and deposited Ca at $2\frac{\mathring{A}}{min}$. The typical 1×3 reconstruction quickly appears and remains for the rest of the growth (up to 10 hours) as shown in Figure 3.3b. The RHEED pattern indicates a similar crystal quality at the co-deposition growth. One disadvantage of the Vogg growth is the inability to determine the thickness of the film because we can't tell what percentage of the Ca is absorbed verse re-evaporated.

When comparing all three growth methods, the Morrar method shows inferior crystal structure. The co-deposition methods has much more control over the film thickness and should be used when precise film control is needed, eg. growth of

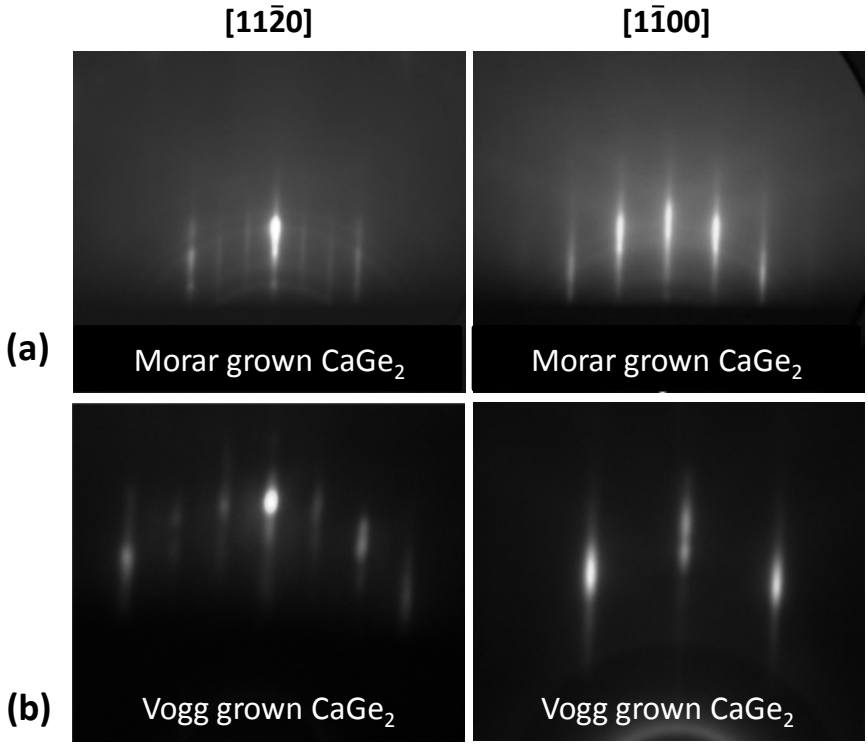

Figure 3.3: (RHEED of $CaGe_2$ grown by the (a)Morar method and (b) the Vogg method

single layer GeH. The Vogg is simpler because there is no rate matching and has the possibility for the incorporation of dopants through the substrate.

3.4 Conversion of $CaGe_2$ to Germanane

Once high quality $CaGe_2$ is grown, it can be converted to GeH using a topotactic transformation. The conversion is accomplished by submersion of the CaGeS films in 37% HCl at -40 °C. The low temperature suppressed the formation of hydroxide leaving hydrogen terminated germanane [8, 73]. Once removed from the HCl the germanane is rinsed with water and methanol for 60 s each.

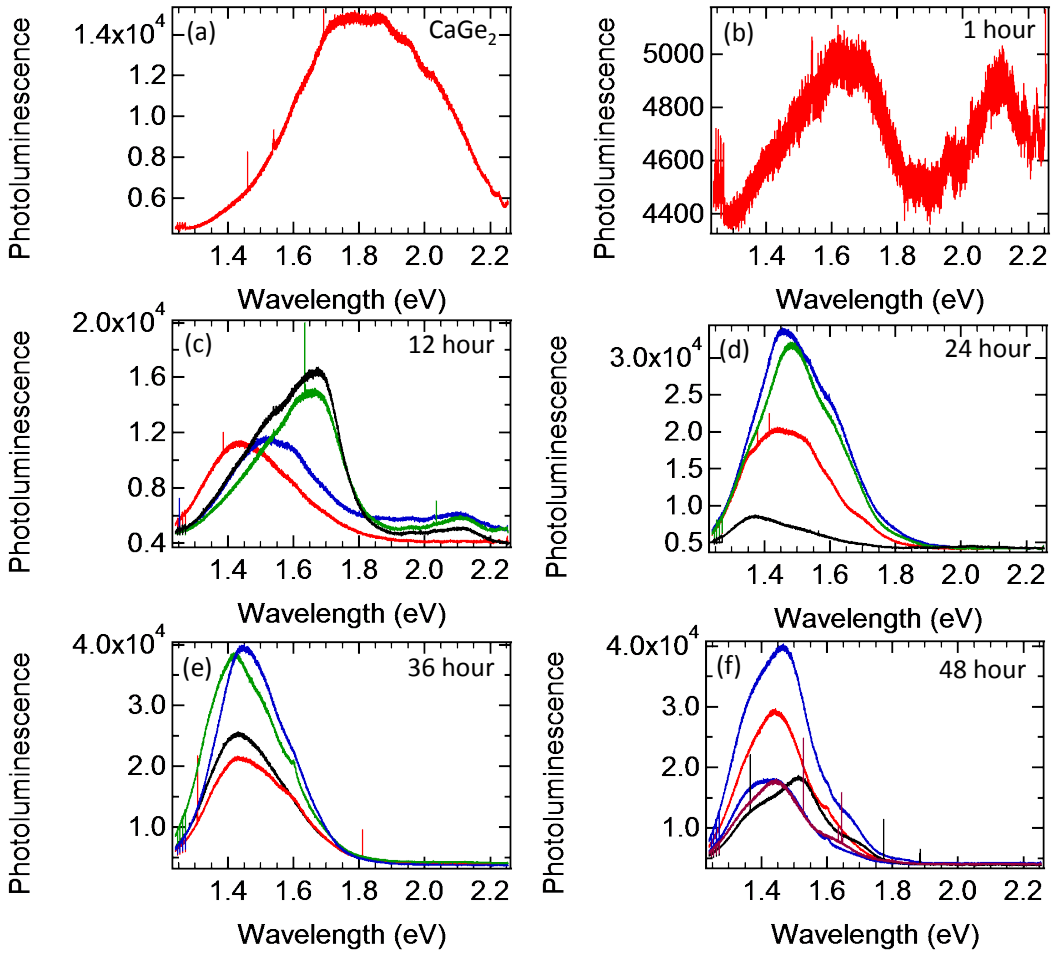

Figure 3.4: (a) Photoluminescence of as grown $CaGe_2$ (b) Photoluminescence of $CaGe_2$ de-intercalated for 1 hour. (c)Photoluminescence take at several different locations of $CaGe_2$ de-intercalated for 12 hours. (d)Photoluminescence take at several different locations of $CaGe_2$ de-intercalated for 24 hours. (e)Photoluminescence take at several different locations of $CaGe_2$ de-intercalated for 36 hours. (e)Photoluminescence take at several different locations of $CaGe_2$ de-intercalated for 48 hours.

While the basic recipe for $CaGe_2$ conversion to GeH is consistent in literature the time left in HCL ranges from 12 hours to 10 days [8, 73]. To calibrate the de-intercalation time, we grew a Vogg style sample where Ca was deposited at a rate of $1 \frac{\text{Å}}{\text{s}}$ for 6 hours. If all of the calcium was incorporated the film thickness would be 720 nm. The film was placed in HCl for times of 0, 1, 12, 24, 36 and 48 hours and was measured by energy-dispersive X-ray spectroscopy (EDS) (Oxford Instruments) and photoluminescence (PL) at 77K. The PL setup is described in section 2.2 of this thesis. We first measured the CaGe2 as grown to give us a baseline. We see large amounts of calcium (11%) and oxygen (51%) in the sample (Table 3.1). The sample also exhibits a broad PL centered at 1.77 eV. We next measure a sample de-intercalated for 1 hour. The PL has become much dimmer and has shifted to 1.65 eV and corresponds to 48% oxygen and 12% calcium. At 12 hours in HCl we no longer see and oxygen peak but the calcium peak remains (9.5%) and a chlorine peak appears(4.4%). The chlorine contamination is consistent with reference [23] The PL is highly dependent on location with the peak ranging form 1.4 to 1.7 eV, suggesting the sample does not de-intercalate evenly. Finally, at 24 hours the calcium goes below detection levels leaving the chlorine (12.6%) as the only contaminant. The PL is stable at $\sim$1.4 which is consistent with reference [73]. Very little changes with the sample de-intercalated for 36 hours. At 24 hours the sample starts to go bad. The PL becomes location dependent varying between 1.4 eV and 1.55 eV. We think that the once the calcium

is removed the HCl starts defecting the germanane. A summary of the EDS data can be found in Table 3.1 and the PL in Figure 3.4.

Table 3.1: Elemental composition of germanane films for various de-intecalation times

	As Grown	1 h	12 h	24 h
Ge	37.27%	39.25%	86%	87.44%
Ca	11.18%	7.23%	9.55%	0%
O	51.54%	48.25%	0%	0%
Cl	0%	0%	4.44%	12.56%

We have determined that there is a window for proper de-intercalation of $CaGe_2$ to become GeH. If you are too short you have calcium contamination. If you go too long you get defects and a increasing amount of chlorine contamination. For the sample studied here the optimum time was between 24 and 36 hours. It is unclear how the thickness of GeH affects the de-intercalation time and should be studied for better results. Also the chlorine contamination sets a limit on the quality of GeH ans should be eliminated to make the GeH of the highest quality.

3.5 Air stability of $CaGe_2$

When GeH is exposed to air it rapidly changes. One can see the surface a GeH film changing from smooth and shiny to rough and dark with a optical microscope (Figure 3.5). The shiny regions disappear after an hour exposure to air. Vogg *et al* [75] show that $CaGe_2$ converts to $Ca(OH)_2(GeH)_2$, which is a Van der Waals material consisting

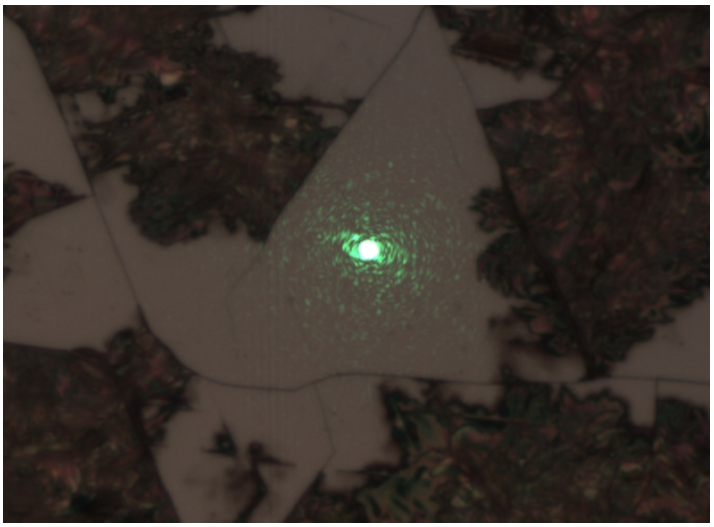

Figure 3.5: Optical micrograph of $CaGe_2$ that has been exposed to air. The surface starts as the shinny white and converts to the rougher red.

of alternating layers of GeH and $Ca(OH)_2$, when exposed to humidity. While $Ca(OH)_2$ etches in HCl, it is unclear how this extra reaction would affect the crystal quality and would be best avoided. To make the $CaGe_2$ air stable a 20 nm Fe cap is grown at room temperature. This cap prevents exposure to air after growth and is removed by the HCl in the de-intercalation process.

3.6 Characterization of germanane grown by Co-deposition

To confirm conversion to GeH we perform x-ray diffraction on a 600 nm thick sample. The θ-2θ x-ray diffraction scan for the resulting film shows two peaks (Figure 3.6a). The peak at $2\theta = 27.3^\circ$ is from the Ge(111) substrate (Figure 3.6a), while the peak at $2\theta = 15.2^\circ$ corresponds to the (0001)-oriented germanane [8]. This confirms that the resulting film is germanane. Figure 3.6d and e show RHEED patterns taken

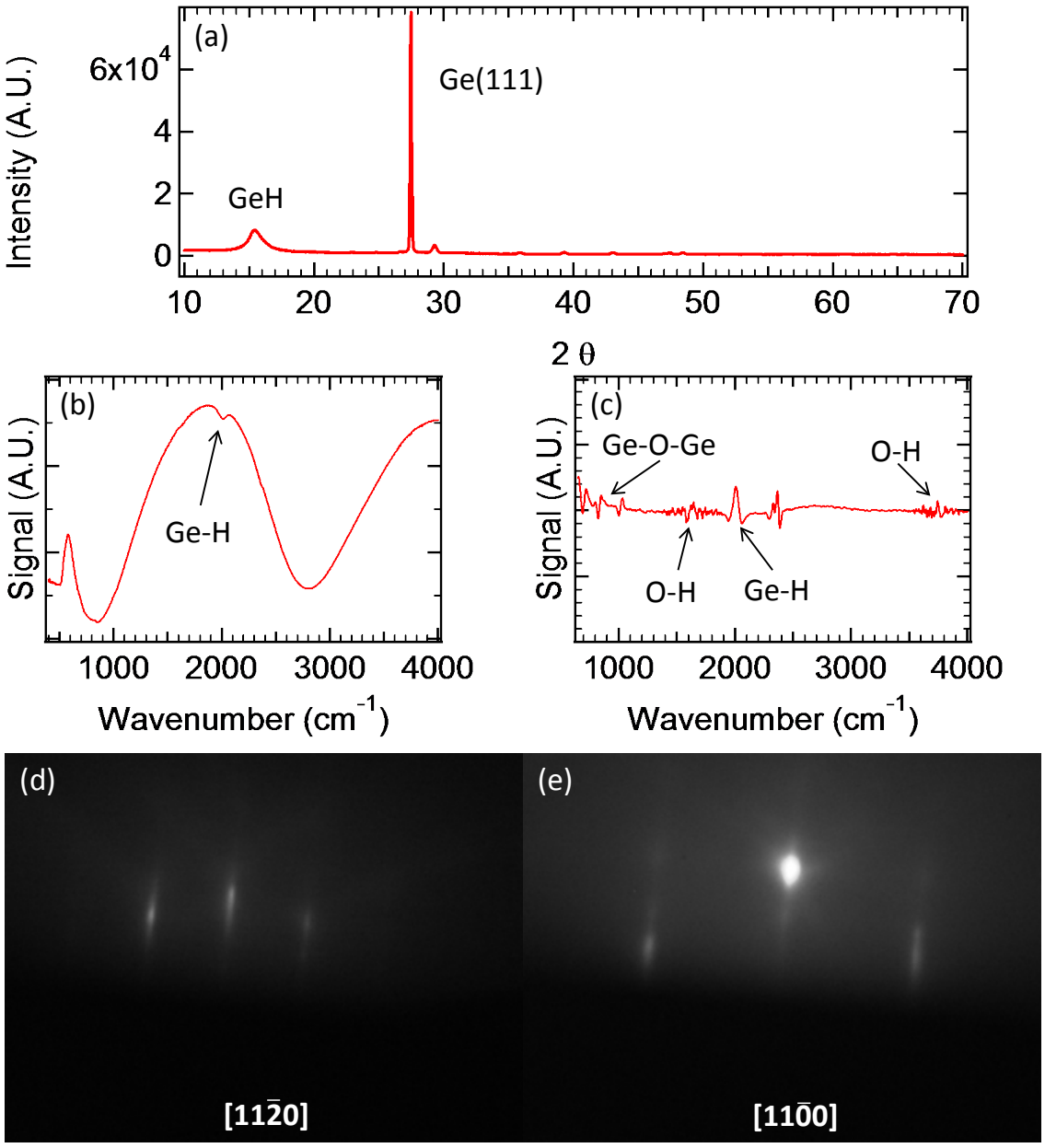

Figure 3.6: (a) θ-2θ scan of 600 nm co-deposited GeH. (b) FTIR scan of 600 nm co-deposited GeH showing a Ge-H mode at 2000 cm^{-1} (c) Second derivative of the FTIR scan in b showing additional Ge-O-Ge and Ge-OH modes. (d) RHEED image of 11$\bar{2}$0 and (e) 11$\bar{0}$0 of de-intercalated GeH.

with beam energy of 15 kV. The diffraction spots form a circular pattern and slide with azimuthal rotation, which indicates a 2D reciprocal lattice. The single RHEED pattern also indicates that the orientation of the germanane film is determined by the underlying Ge(111) substrate.

Out GeH films were further characterized using FTIR spectroscopy (Bruker). Two features of the FTIR spectrum (Figure 3.6b) are immediately obvious. First there is a large sinusoidal background due to the thin film nature of the sample. Second, there is a dip at $\sim$2000 cm^{-1} corresponding to the Ge–H strech vibrational modes. The further elucidate any small peaks in the signal we perform a second derivative analysis (Figure 3.6c). Here we see the Ge–O–Ge vibrational modes between 800–1000 cm^{-1}, and O–H bend and stretch modes at 1300–1700 cm^{-1} and 3300–3600 cm^{-1} respectively [8, 73]. It is important to note that while we do see some evidence of oxidation it is very small.

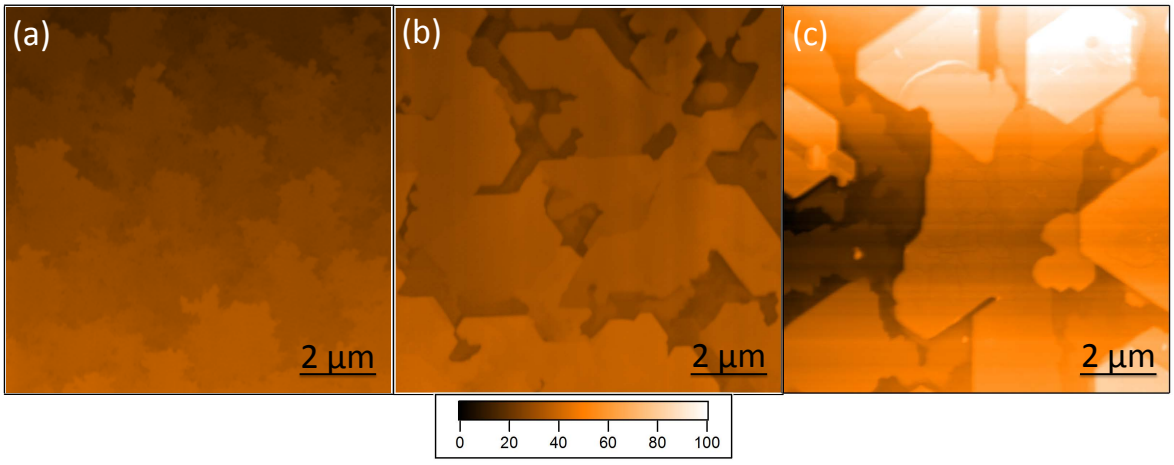

Figure 3.7: (a) AFM of Ge buffer layer annealed at 750 ° (b) AFM of 5 nm $CaGe_2$ (c) AFM of 5 nm GeH

To investigate the morphology of the film, we perform *ex situ* AFM measurements on a thin 5 nm $CaGe_2$ film before and after de-intercalating in HCl (Figure 3.7). For reference, we show an AFM scan of a 5 nm Ge buffer layer on a Ge(111) substrate taken from the same wafer Figure 3.7a. This Ge buffer layer is grown at 650 °C and then heated to 750 °C to reproduce the conditions just prior to the $CaGe_2$ deposition. AFM of the Ge buffer layer shows the formation of terraces due to the miscut of the Ge(111) substrate. The typical height of each terrace is $\sim$5 nm. Figure 3.7b shows that with the growth of 5 nm $CaGe_2$, the terrace size becomes larger. This indicates the propensity for the $CaGe_2$ to grow flat on the (111) plane. To maintain the global miscut of the substrate, the terrace height also increases to typical values of $\sim$10 nm (note that a terrace width of a few micrometers and height of $\sim$10 nm corresponds to a miscut of $\sim 0.2^{\circ}$). After de-intercalation Figure 6c, the overall terrace size is similar to the $CaGe_2$ film. To determine the local roughness of the film, we analyze the rms roughness within individual terraces. We find that the Ge buffer has rms roughness of 0.26 nm, the $CaGe_2$ film has rms roughness of 0.40 nm, and the germanane film has rms roughness of 0.25 nm. Most importantly, even after submerging in HCl solution to obtain germanane, the individual terraces remain atomically smooth

3.7 Conclusion

We have demonstrated the successful co-deposition of $CaGe_2$ films on Ge(111) by MBE. The growth occurs within an adsorption-limited growth regime with over-pressure of Ca, which ensures stoichiometry of the film. The best RHEED patterns are obtained at a growth temperature 750 °C. The $CaGe_2$ films are then immersed in hydrochloric acid and subsequent characterizations by x-ray diffraction and FTIR spectroscopy indicate that the resulting film is germanane. RHEED patterns indicate that the crystalline orientation of the germanane film is determined by the underlying Ge(111) substrate. Furthermore, both RHEED and AFM measurements indicate that the local morphology is smooth at the atomic scale. However, the grain size is limited to a few micrometers, primarily due to the miscut of the Ge substrate. Thus, optimization of the substrate could yield much larger grain sizes. These results provide a significant advance toward the long-term goal of developing large area germanane.

Chapter 4

Large Area Germanane on Arbitrary Substrates

Parts of this chapter were adapted form reference [1]. This was a collaborative work with many of the Kawakami group students participating. Specifically Walid Amamou and I developed the transfer process and the subsequent characterization. Walid Amamou performed the electrical measurements and Elizabeth Bushong performed the wavelength dependent photo conductivity.

4.1 Introduction

Recently, large area germanane films have been synthesized by growing Zintl-phase $CaGe_2$ thin films on Ge(111) wafers by molecular beam epitaxy (MBE) [58]

or substrate reaction [73, 74], followed by chemical processing in acid solution to convert the $CaGe_2$ into hydrogen-terminated germanane (GeH). In order to utilize this material for electronic devices, it is necessary to transfer the GeH film to an insulating substrate to prevent parallel conduction paths. In addition, a transfer process will allow the integration of GeH into vertically stacked heterostructures with other 2D materials. In this study, we report the large area transfer of epitaxial GeH by electrochemical delamination (i.e. "bubble transfer") and demonstrate electron transport and photoconductivity. We are able to reliably transfer films up to 1 cm^2, which is limited by the size of our sample holder. The photoluminescence (PL) spectra and the x-ray diffraction scans (XRD) remain largely unchanged by the transfer process, indicating that the optical and bulk structural properties are maintained. Furthermore, energy-dispersive X-ray spectroscopy (EDS) shows no residual electrolyte (within measurement sensitivity) remaining from the transfer process. We investigate electron transport and photoconductivity by transferring to insulating substrates and depositing metallic electrodes through shadow masks. In particular, photoconductivity of few-layer GeH exhibits an absorption edge as a function of wavelength as expected for a semiconductor. Because most other techniques for characterizing germanane have required thick films or bulk crystals, the demonstration of photoconductivity measurements on few layer GeH is very important for the further optimization and development of ultrathin germanane materials.

4.2 Large Area Transfer

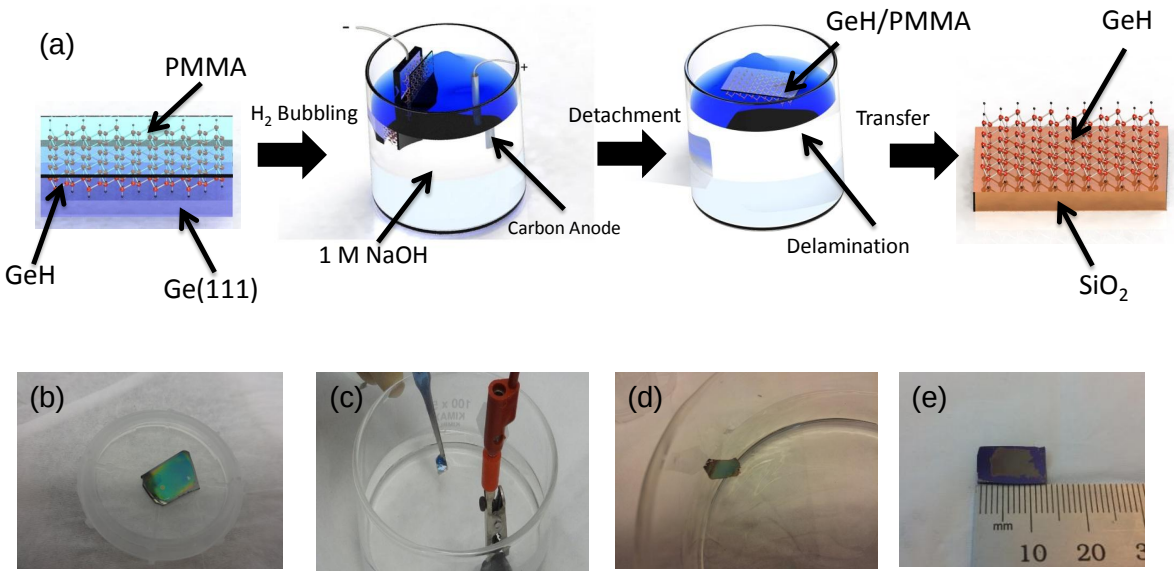

Figure 4.1: (a) Schematic of the transfer process, (b) Optical image of PMMA/GeH/Ge(111), (c) Optical image of the electrochemical cell, (d) Optical image of the floating PMMA/GeH film (e) Optical image of GeH transferred to SiO2.

To realize germanane-based electronic devices, it is necessary to transfer the GeH film to an insulating substrate. Our initial attempts at transferring the GeH film included mechanical exfoliation using various tapes and polydimethylsiloxane (PDMS) stamping procedures. However, these methods resulted in low yield and small flake size (< 10 μm). A popular method for transferring large area 2D films is to support the film with polymer and etch away the underlying substrate, which is commonly used to remove copper foil from CVD graphene [31]. However, we are not aware of a selective etch that differentiates between GeH and Ge. Therefore, we focus our

attention to electrochemical delamination based on water electrolysis, i.e. bubble transfer [14, 78], which has been effective for transferring other 2D materials.

Figure 4.1a illustrates the main steps for the bubble transfer and Figures 4.1b-4.1e are photographs taken during the process. Beginning with a GeH film on a p-type Ge (111) substrate (Figure 4.1b), we spin coat the sample with polymethylmethacrylate (PMMA) at 2000 rpm for 45 sec and then bake at 50 °C for 2 hr. The PMMA coating of GeH provides structural support during the delamination process. To facilitate detachment during the water electrolysis, the PMMA on the edge of the substrate is removed with acetone. Then, we dip the PMMA/GeH/Ge(111) cathode and a graphite anode into a 1M NaOH aqueous solution and slowly increase the current at a typical rate of $\sim$0.01 $\frac{\text{A}}{\text{s}}$ (Figure 4.1c) until the PMMA/GeH starts to detach. The current produces H_2 bubbles at the interface between the PMMA/GeH and the Ge(111) due to water reduction $2H_2O_{(l)} + 2e^- \rightarrow H_{2(g)} + 2OH^-_{(aq)}$. The hydrogen bubbling time necessary to detach the PMMA/GeH layer from the Ge substrate depends on the size of the film and the current applied. Typically, after approximately 10 s of bubbling, the PMMA/GeH layer floats to the top of the NaOH solution (Figure 4.1d). The corresponding electrolyte voltage is approximately 5 V with a current of $\sim$0.06 A for a 1 cm^2 sample. The PMMA/GeH is then moved to a bath of de-ionized (DI) water for 15 min to remove the remaining electrolytes from the sample. After cleaning, we transfer the PMMA/GeH layer to the desired substrate and bake on a hot plate at 50 °C for 10 min to help remove the interfacial water layer. The residual

PMMA is removed by immersing the transferred sample in acetone at 50 °C for 30 min, followed by an isopropanol rinse for one minute to remove the acetone. Finally, we dry the sample with nitrogen gas. Figure 4.1e shows a transferred film with a size of several mm.

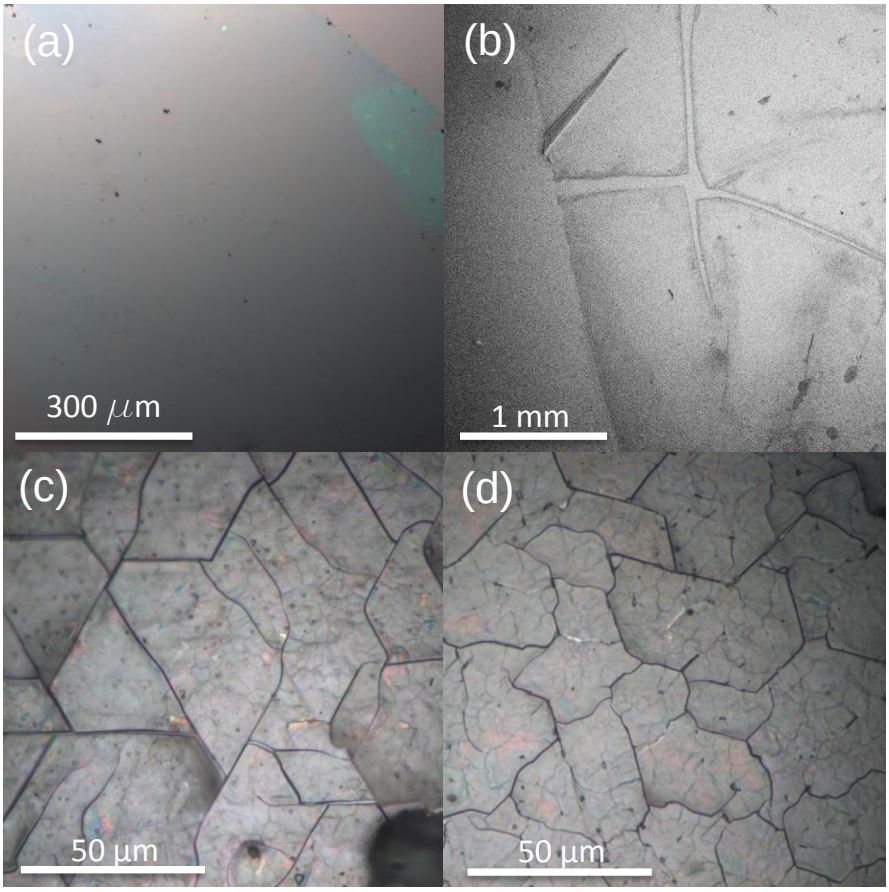

Figure 4.2: (a) Optical micrograph of 5 nm GeH transferred to SiO2, (b) SEM image of 5 nm GeH transferred to SiO2, (b) Optical micrograph of 600 nm as grown GeH on Ge(111), (d) Optical micrograph of 600 nm GeH transferred to SiO2.

We have successfully transferred GeH films between 1 nm and 600 nm thicknesses to arbitrary substrates. Figure 4.2 shows optical and scanning electron microscope (SEM) images of 5 nm GeH films transferred to a SiO2(300 nm)/Si substrate. The

optical image (Figure 4.2a) shows a continuous large area of GeH. The upper right corner of the image shows the edge of the film, which is visible due to color contrast with the bare substrate. The SEM image (Figure 4.2b) shows continuous regions larger than $\sim$1 mm and separated by tears, which produce enhanced contrast between the substrate and film. The continuous regions are typically larger and exhibit fewer features. For the thicker GeH, we observe similar cracking before transfer (Figure 4.2c) and after transfer (Figure 4.2d), which shows that the morphology is conserved.

4.3 Characterization of transfered germanane

To determine the effect of the bubble transfer on the quality of GeH films, we perform a series of characterization measurements before and after transferring. To minimize substrate-related effects, we transfer the GeH film from its original Ge(111) substrate to another Ge(111) substrate. The out-of-plane lattice spacing was analyzed using XRD on a 600 nm GeH film. Before transfer, we observe a peak at $2\theta = 15.8^{\circ}$ which corresponds to the GeH layer spacing of 5.7 Å, Figure 4.3a. As shown in Figure 4.3b, the position and line width of the GeH peak are preserved after transfer, indicating that the transfer does not produce major changes to the crystal structure.

To investigate the effect of bubble transfer on optical properties, we perform PL spectroscopy at low temperatures (10 K). PL is performed using a 532 nm laser ex-

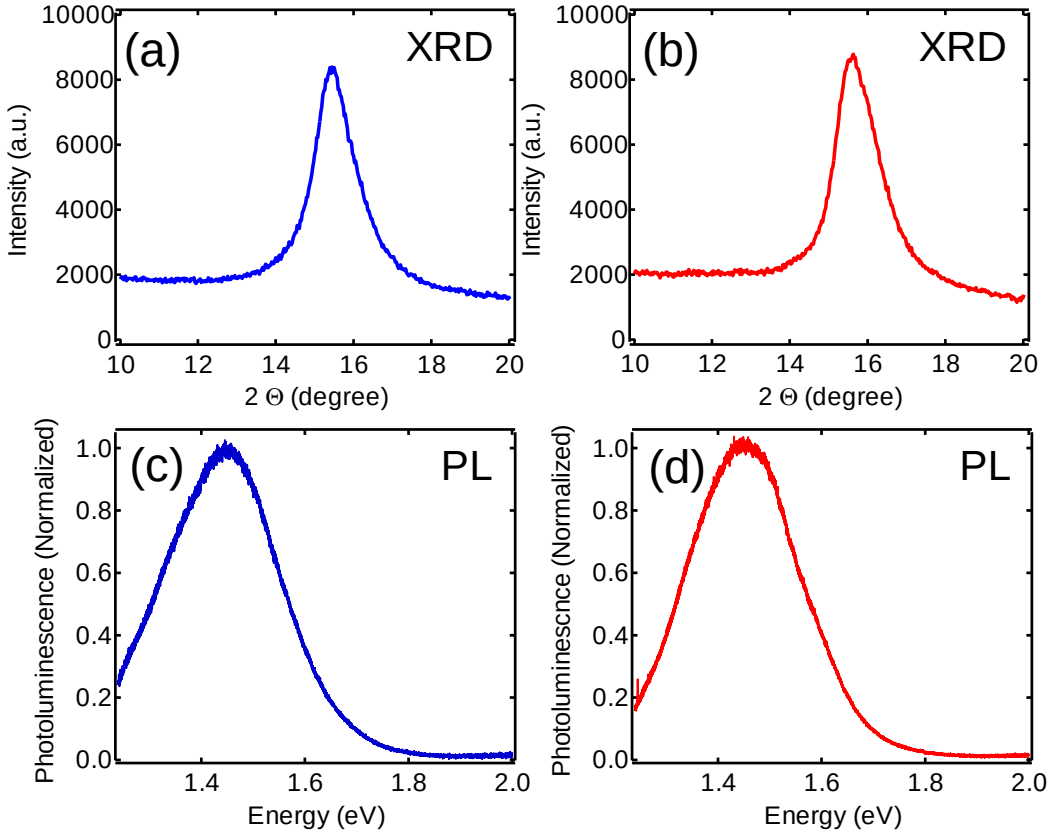

Figure 4.3: (a) XRD of as-grown 600 nm GeH film, (b) XRD of transferred 600 nm GeH film, (c) PL of as-grown 600 nm GeH film, (d) PL of transferred 600 nm GeH film.

citation (1 mW, 20 μm spot size) and the spectra are captured using a 0.5 meter Czerny-Turner spectrometer with a liquid nitrogen cooled CCD camera (Princeton Instruments). A white light source (tungsten lamp modeled as a blackbody) is used to calibrate and correct for the wavelength dependence of the detector efficiency. The PL spectrum before transfer exhibits a peak at $\sim$1.45 eV (Figure 4.3c), which is consistent with previous reports of PL on epitaxial GeH [73]. After transfer, the PL spectrum again exhibits a peak at $\sim$1.45 eV and the intensity is not degraded (Figure

4.3d). Notably, we did not observe photoluminescence at ∼1.9 eV, which is reported to occur in the presence of oxidation [73]. This suggests that the bubble transfer of GeH does not promote oxidation and preserves the optical quality.

Table 4.1: Elemental composition of germanane films by EDS

	10 keV As Grown	20 keV As Grown	20keV Transfered
Ge	71.6%	92.77%	92.82%
Cl	11.16%	7.23%	7.18%
O	17.24%	0%	0%

Finally, we have examined the possible contamination of the sample during the transfer using EDS spectroscopy (Oxford Instruments) in an SEM at 20 kV. The spectrum before transfer shows a strong Ge signal and no observable Ca and O signals. In order to probe the surface, we performed low energy (10 kV) EDS and observed some surface oxidation. The Cl remaining in the material after deintercalation is about 7%, similar to what has been reported previously [23, 73]. After transfer, the 20 kV EDS spectra was free of Na and O signals. The data is summarized in Table 4.1. This confirms that the bubble transfer introduces little or no contamination (below detection limits) to the GeH film.

4.4 Electron transport and photoconductivity

To investigate the electrical and photoconductive properties of GeH films on the SiO_2(300 nm)/Si substrate, we deposit metallic electrodes through shadow masks.

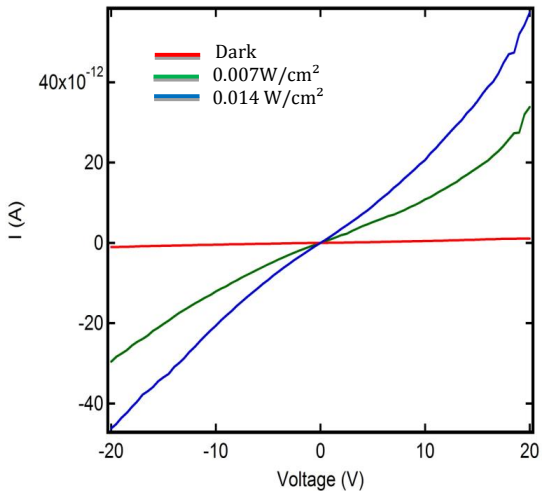

Figure 4.4: IV of 100nm Germanane illuminated by different intensity 635 nm light

For thicker films (>50 nm), we utilize a shadow mask with fine features in order to have a continuous conduction channel in between the cracks. Figure 4.5a is an optical microscope image of a 600 nm GeH film with Au/Ti electrodes separated by 20 μm. DC photoconductivity is measured by applying a voltage between the drain and source and measuring the current under illumination by a 635 nm laser. A factor 50 increase in current from dark is seen when illuminated by 0.014 $\frac{\mathrm{W}}{\mathrm{cm}^2}$ 635 nm light (Figure 4.4).

Wavelength dependent AC photoconductivity measurement is performed using pulsed laser excitation (150 fs, 76 MHz repetition rate) from a Ti:sapphire oscillator (700 nm – 960 nm wavelength range) or optical parametric oscillator (520 nm – 740 nm wavelength range). The laser beam is maintained at a power of 1.0 mW and has a beam diameter of 2 mm. The beam is incident on the device without a focusing lens, thereby producing a broad illumination with an intensity of 0.03 $\frac{\mathrm{W}}{\mathrm{cm}^2}$. The beam

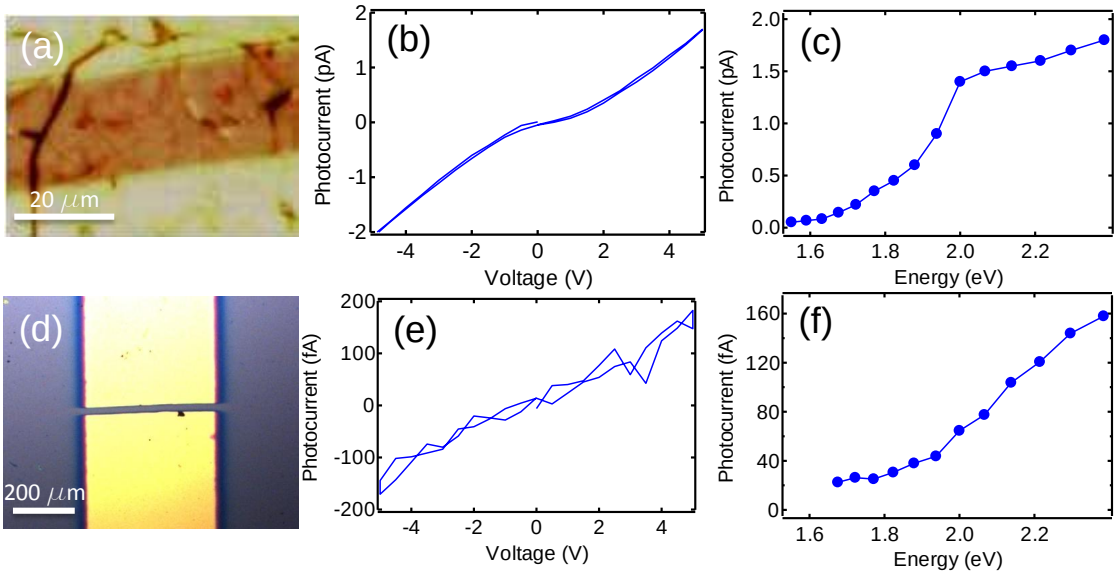

Figure 4.5: (a) Optical micrograph of a 600 nm GeH device, (b) Bias dependence of photocurrent for the 600 nm GeH device illuminated by 540 nm light, (c) Wavelength dependence of photocurrent at 5 V bias for the 600 nm GeH device, (d) Optical micrograph of a 5 nm GeH device, (e) Bias dependence of photocurrent for the 5 nm GeH device illuminated by 540 nm light, (f) Wavelength dependence of photocurrent at 5 V bias for the 5 nm GeH device.

is chopped at a frequency of 493 Hz and the resulting photocurrent is pre-amplified and measured by lock-in detection. All photocurrent measurements are performed at room temperature

Figure 4.5b shows the photocurrent of a 600 nm GeH device as a function of bias voltage for a laser wavelength of 540 nm. The bias voltage is ramped from 0 V to +5 V to -5 V to 0 V to detect possible hysteretic effects as a function of bias voltage. The photocurrent vs. voltage curve exhibits no hysteresis and is slightly nonlinear. We investigate the wavelength dependence of the photocurrent by adjusting the laser wavelength and repeating this measurement every 20 nm. Figure 5c summarizes the wavelength dependence by plotting the photocurrent at +5 V bias. At low photon en-

ergies, there is little photocurrent because the photon energy is below the band gap. As the photon energy is increased, more photons are absorbed and the photocurrent increases. This behavior is typical of a semiconductor, where the absorption rapidly increases as the photon energy exceeds the band gap and is similar to recent measurements on bulk germanane crystals [2]. We note that this photocurrent spectrum is also similar to previous optical reflectance spectroscopy performed on epitaxial GeH/Ge(111) [16].

Next, we investigate photoconductivity of thin GeH devices. For these devices, we added an extra step in the synthesis procedure, in which we grew a Fe cap on the $CaGe_2$ film prior to deintercalation to reduce potential oxidation of the $CaGe_2$ layer. Because these films are continuous, we deposit larger metallic electrodes of width 400 μm and separated by a 20 μm gap. Figure 4.5d is an optical microscope image of such a device with GeH film thickness of 5 nm (a few layers of GeH). Figure 4.5e shows the photocurrent of this device as a function of bias voltage under laser illumination at 540 nm. There is an order of magnitude less photocurrent for this device compared to the thick GeH and the signal is approaching the level of the noise. Nevertheless, the photoconductivity can still be determined reliably by linear fitting of the data. The photocurrent spectrum shown in Figure 4.5f displays the expected behavior for a semiconductor, with low photocurrent at low photon energies and an increase of photocurrent with increasing photon energy. Although the absorption edge appears to have shifted to slightly higher energies compared to the thick device

(Figure 4.5c), the overall features of the photoconductivity spectra are similar. We have also observed photoconductive signals in 1 nm GeH films.

The ability to measure these weak photoconductivity signals is very important for the optimization of few-layer germanane films. Up to now, the most important materials characterizations such as XRD and PL could only be applied to thick GeH films due to the lack of measurable signal in the thinner films. Now with the photoconductivity measurement, we have a means of characterizing the electronic and optical properties of few-layer germanane and can use this information to optimize the material synthesis procedures.

4.5 Conclusion

We developed the large area bubble transfer of GeH onto arbitrary substrates. This is an important advance, as the bubble transfer of GeH enables the fabrication of electronic devices on insulating substrates, optical studies on transparent substrates, as well as the creation of vertically stacked 2D heterostructures. We verified that the structural and optical properties of thick GeH films are largely unchanged by the transfer process with PL and XRD. Additionally, the transfer process does not contaminate the thick GeH films with residual electrolytes (within measurement sensitivity), verified with EDS spectroscopy. Once transferred, GeH films were fabricated into two-terminal devices to allow transport measurements and photoconductivity

measurements. The photoconductivity of both thick and few-layer GeH indicates an absorption edge as a function of wavelength, as expected for a semiconducting material. The photoconductivity measurements on few-layer GeH are particularly important for the further optimization and development of ultrathin germanane materials. These results represent a major advance toward the realization of electronic and optoelectronic technologies in this emerging 2D material.

Chapter 5

Optical Properties of Germanane

This was a collaborative work with many of the Kawakami and Crooker group members participating. Specifically I performed the PL, PLE, Absorption and TCSPC measurements. Elizabeth Bushong performed the WDPC. Walid Amamou and Dante O'hara grew the samples.

5.1 Introduction

In order for germanane's exciting properties to be realized, several fundamental properties such as band edge and carrier lifetime need to be studied. To date there have been no systematic study on MBE grown germanane films. Theory calculations predict that the band edge is between 0.96 and 3.6 eV [8, 16, 20, 37, 39]. The large range of theoretical values makes an experimental determination of the actual value very important. Carrie lifetime is another useful property that has no experiment.

In this chapter, I present temperature dependent photoluminescence (PL) and study the band edge of germanane using photoluminescence excitation spectroscopy (PLE), absorption and wavelength dependent photo-conductivity (WDPC). Time correlated single photon counting (TCSPC) measurements reveal the electron dynamics.

5.2 Photoluminescence

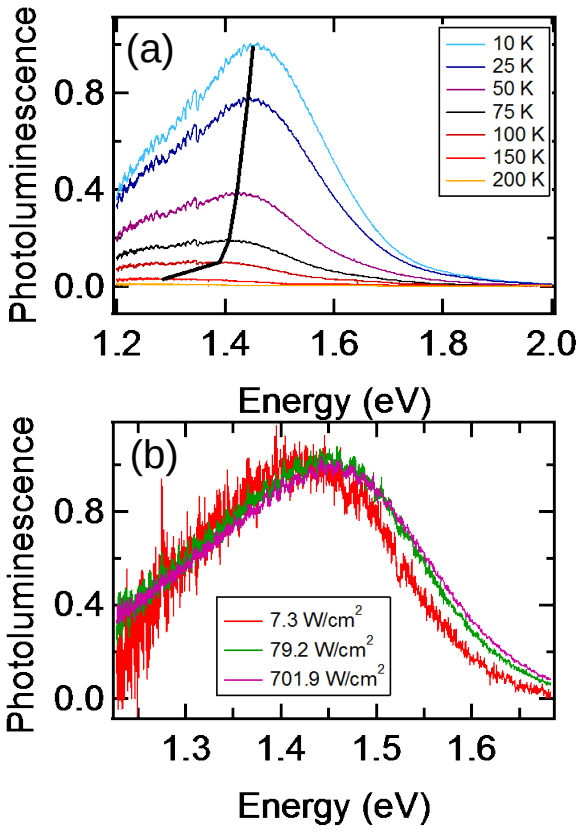

Figure 5.1: (a)Temperature dependent PL of a 600 nm germanane sample. The black lines indicate the shift in peak center with temperature (b) Normalized power dependent PL showing and broadening and shift to higher energy with increasing excitation intensity

The optical properties of germanane were first studied using temperature dependent photoluminescence. The samples were illuminated using 200W/cm_2 of 532 nm light and the luminescence was measured using an imagine spectrometer (Roper Scientific) with a liquid nitrogen cooled CCD detector (Princeton Instruments). The spectral response and etalon modes of the detector were corrected using a white light. No photoluminescence is observed at room temperature (RT) which is consistent with reference [73]. At 10 K a broad luminance is seen centered around 1.45 eV. As temperature increases the peak gradually red shifts getting broader and dimmer until photoluminescence completely disappears between 200 and 250 K depending on sample as seen in Figure 5.1a. Also it is to be noted that photoluminescence is not observed on samples below 100 nm. Reference [74] indicates this due to a structural change around that thickness.

A 424nm laser was used to study the intensity dependence of photoluminescence at 10 K between powers of 7 and 700 W/cm2. As seen in Figure 5.1b the photoluminescence peek broadens and blue shifts by $\sim$30 meV. One possible explanation for this is that the photoluminescence we are observing is due to defects whereas the excitation intensity is increased more defect states are filled leading to higher energy states being filled causing a broadening and blue shift of the photoluminescence. Defect photoluminescence would be consistent with the broad luminescence observed.

5.3 Photoluminescence excitation spectroscopy

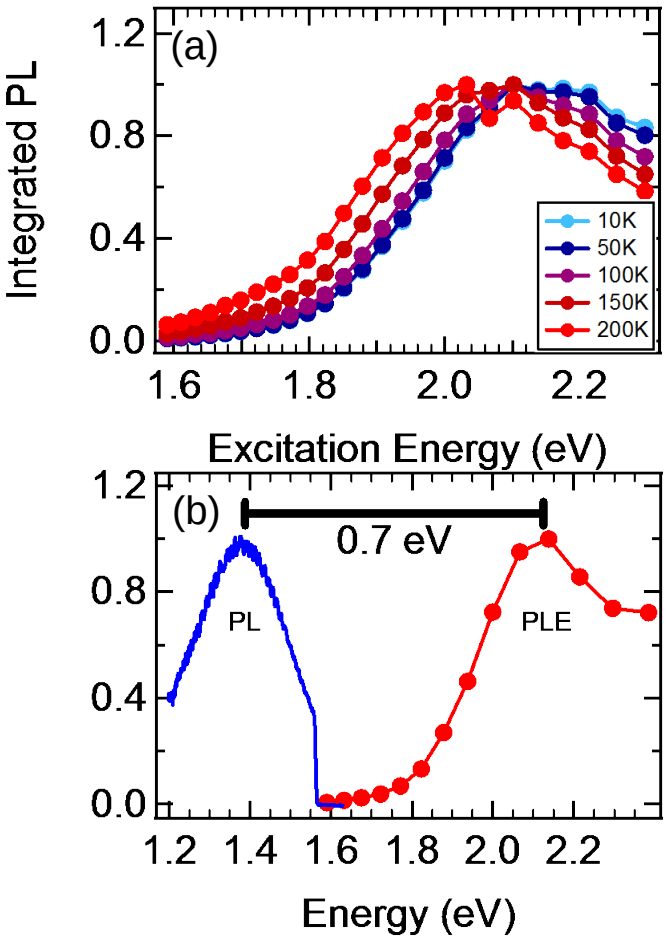

Figure 5.2: (a)Temperature dependent PLE of a 600 nm germanane sample. (b) PLE and PL showing the large stokes shift between the two.

Since germanane exhibits photoluminescence, photoluminescence excitation spectroscopy (PLE) can be used to study the absorption edge. A tunable light source was created using a xenon arc lamp (Energetiq) and Czerny Turner monochromator (Roper Scientific) and had a full width half max (FWHM) of 10 nm. The resulting photoluminescence was measured with the same setup used for the previous mea-

surements. Photoluminescence was then taken at several excitation wavelengths, integrated and normalized to the excitation power. The integrated photoluminescence scales with power over the range used for the PLE measurement. The PLE measurements reveal a large Urbach tail of several hundred meV with a peak near 2.1 eV at 10 K (Figure 5.2a). The large Urbach tail is a sign of defects [65]. As temperature is increased the PLE maxima red shifts as expected for semiconductors. The size and shape of the Urbach tail remains unchanged with temperature (figure XXX). As seen in figure 5.2b, the PL peak and the PLE maximum are stokes shifted by $\sim$700 meV. This large shift could be explained by defect photoluminescence. Large binding energies have been predicted for germanane though we observe no evidence of a bound state [60].

5.4 Absorption

We next measure transmittance on a 20 nm sample of germanane transferred sapphire by the electrochemical delamination method described in Chapter 4. Here white light was focused through the germanane sample and the transmitted light was measured using spectrometer (Princeton Instruments). The mass absorption coefficient (α) was calculated using the Beer-Lambert law, $I = I_0 e^{-\alpha d}$, where I_0 is the incident spectrum, I is the transmitted spectrum and d is the film thickness [88]. To account for the sapphire substrate, I_0 was taken to be the spectrum transmitted

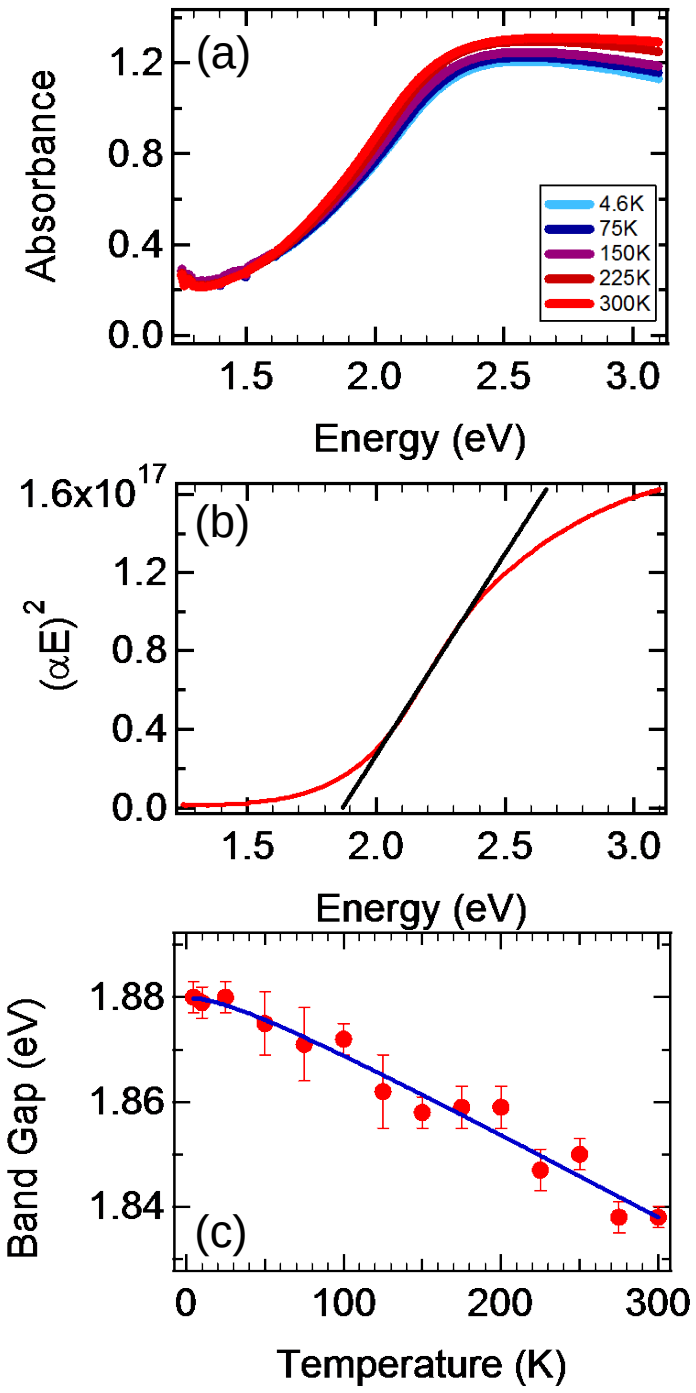

Figure 5.3: (a)Temperature dependent ansorbance of a 20 nm germanane sample. (b) Plot showing the fitting of absorbance to get the band edge. (c) Plot of the temperature dependence of the band edge fit by the Varshni equation (blue)

through the sapphire and I was taken to be the spectrum transmitted through the sapphire and germanane film. As seen in Figure 5.3a the mass absorption coefficient has a similar shape as the PLE with a large Urbach tail indicating defects. The absorption edge shifts to lower energy with increasing temperature as expected for a semiconductor.

Using the Tauc equation, $\alpha h\nu = B(h\nu - E_g)^m$, we can fit the absorption data and extract the band edge [2]. Here hn is the photon energy, B is a phenomenological constant, E_g is the bandgap energy and m is parameter changed for the type of gap. We use m=1/2 as germanane is a direct gap semiconductor. To extract the band edge $(\alpha h\nu)^2$ is plotted verse $h\nu$. The linear region is then extrapolated to the x axis and the x intercept gives you the bandgap energy (Figure 5.3b). At 4.6 K, the bandgap is found to be 1.88 eV. This is higher than the room temperature measurements given is ref [8]. The fitted bandgap red shifts with increasing temperature and the shift can be well described by the Varshnis empirical equation describing the shift of bandgap with temperature (Figure 5.3c).

5.5 Wavelength dependent photo-conductivity

To gain insight on whether the absorption is from a band like state or localized defects, WDPC measurements are performed. Wavelength dependent AC photoconductivity measurement is performed using pulsed laser excitation (150 fs, 76 MHz

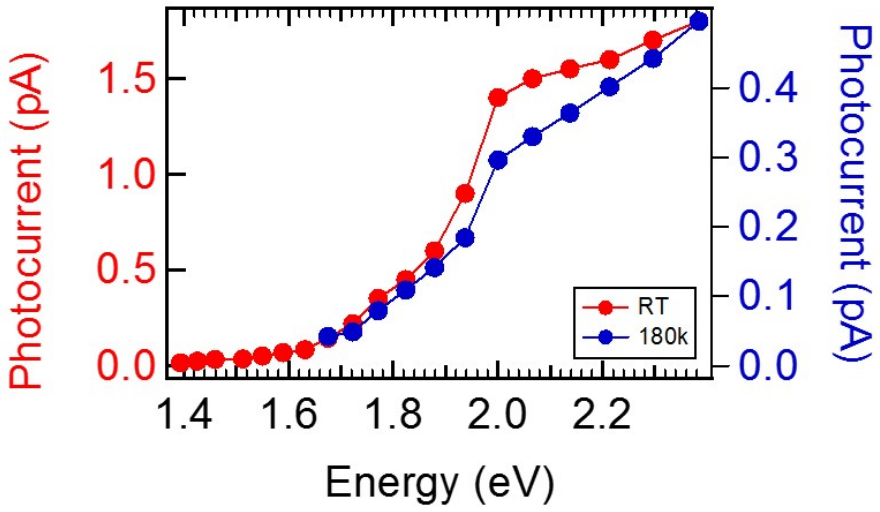

Figure 5.4: WDPC at room temperature (blue) and 180K (red)

repetition rate) from a Ti:sapphire oscillator (700 nm – 960 nm wavelength range) or optical parametric oscillator (520 nm – 740 nm wavelength range). The laser beam is maintained at a power of 1.0 mW and has a beam diameter of 2 mm. The beam is incident on the device without a focusing lens, thereby producing a broad illumination with an intensity of 0.03 W/cm_2. The beam is chopped at a frequency of 493 Hz and the resulting photocurrent is pre-amplified and measured by lock-in detection. The photocurrent is measured with a +5V bias for several wavelengths. WDPC shows the same absorption edge as the PLE and absorption measurements that is dominated by a large Urbach tail (Figure 5.4). Temperature dependence shows a blue shifting with decreasing temperature as well as an increase in resistance. Due to germanane high resistance WDPC measurements are not possible below 180 K. As WDPC probes changes in conduction we can rule out the absorption edge is due to highly localized states and must be dues to a band like state.

5.6 Time correlated single photo counting

Finally the carrier lifetime was measured using TCSPC. A pulsed 645 nm laser (14 uW, 200 kHz, PicoQuant) was used to excited the germanane. The resulting photoluminescence was measured using a single photon avalanche photodiode (SPAD) with a time resolution of 1ns (Excelitas Technologies). Time correlation between the laser pulse and the first detected photon was performed using the Picoharp 300 (PicoQuant). Figure 5.5a shows the TCSPC measurement on 200 nm of germanane at 4 K. The decay curve is a combination of many different lifetimes ranging from a few ns to a few s. One explanation is that the PL is from many defect centers that each has a different electronic lifetime. As seen in Figure 5.5b, the fast dynamics of the TCSPC signal does not track the instrument response of the SPAD indicating that this fast dynamic is not an artifact of the system. Temperature dependent measurements were performed up to 150 K and show little change (Figure 5.5c). Due to the noise resolution in the slow decay component, is possible that there is some change that can't be resolved. Wavelength resolved measurements were performed by putting a monochromator (Roper Scientific) before the SPAD. Measurements were taken at 1.5, 1.46, 1.42, and 1.38 eV with a resolution of 10 nm. No trend was seen between the different energies.

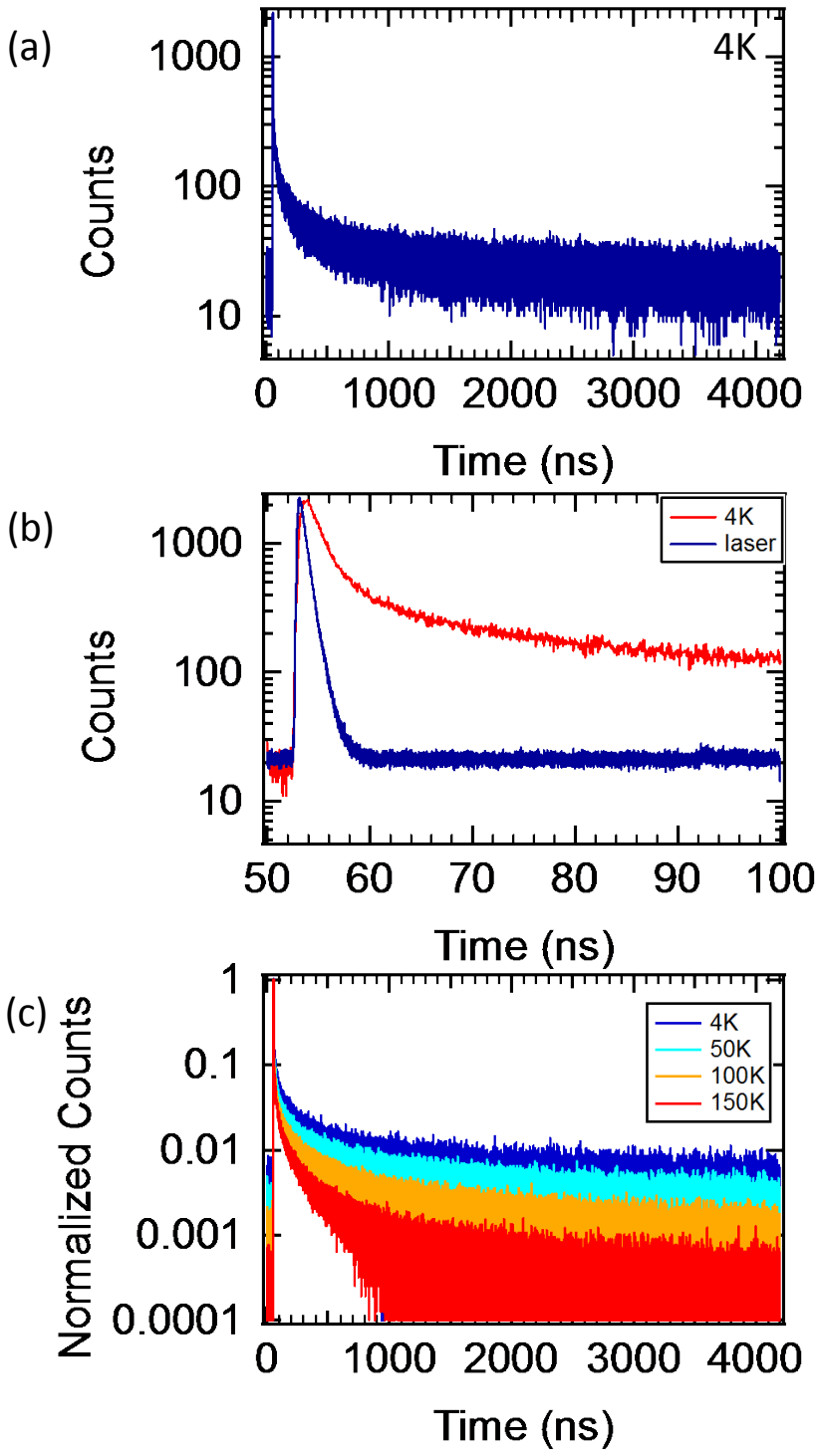

Figure 5.5: (a) TCSPC of 200 nm of GeH at 4 K. (b) The fast dynamics of of GeH at 4 K (red) compared to the time resolution of the SPAD (blue) measured by reflecting the pulse laser into the SPAD. The difference of the signals indicates the fast dynamics are not an artifact of the system. (c) Temperature dependent TCSPC. There is no change in the fast dynamics and the slow dynamics are dominated by noise.

5.7 Conclusion

A coherent study on germananes optical properties has been presented. Photoluminescence is observed at 1.45 eV at 10k which is consistent with reference XXX and red shifts with increasing temperature. Power dependent PL indicates that the PL is due to defects; which is supported by the large Urbach tail seen in the absorption measurements. Fitting of absorption measurements indicate a bandgap of 1.88 eV which is consistent with PLE and WDPC measurements. This number is higher than previous reported values of 1.6 and 1.7 eV [8, 16]. This is partially due to differences in temperature at which the measurements are taken as well as differences in materials quality. WDPC show that the absorption occurs in a state the conducts indicating that it is band like and not localized.

Chapter 6

Controlled argon beam-induced desulfurization of monolayer molybdenum disulfide

This chapter was adapted from reference [38]. This was a collaborative work with many of the Kawakami and Bartels group members participating. Quan Ma developed the sputtering process and performed the XPS measurements. Quan Ma and I developed the *in situ* PL measurement. John Mann grew the samples and Duy Le provided computational assistance.

6.1 Introduction

Like graphene, single-layer MoS_2 is stable in air for extended periods of time. In carbon-based materials, such as nanotubes and graphene, this high stability, while attractive for many purposes, has proven a challenge for other needs. Intense processing is required, for example, to bond covalently to these materials, to render them soluble, and to alter their electronic properties, such as by hydrogenation or partial oxidation of graphene. For MoS_2, the inertness of the basal plane calls for interventions to facilitate chemical reactions. In this regard, theoretical studies indicate that sulfur vacancies are reactive [4, 43]. In this study we show that sputtering with low-energy Ar^+ ions can transform single-layer MoS_2 all the way to $MoS_{1.5}$, while in situ x-ray photoelectron spectroscopy (XPS) reveals substantially unchanged Mo 3d states. In situ monitoring of the photoluminescence (PL) allows us to gauge the impact of the sputter-induced defects/vacancies on the exciton dynamics; in the temperature regime between 175 and 300 K we find a decay of PL yield that decreases at $\sim$7.0$\pm$0.5 times the rate of sulfur removal.

6.2 Methods

Our measurements were performed on films and isolated islands of single-layer MoS_2 grown on a SiO_2 substrate from MoO_3 and elemental sulfur, as described elsewhere [44]. Figure 6.1a shows an optical microscopy image of a representative area

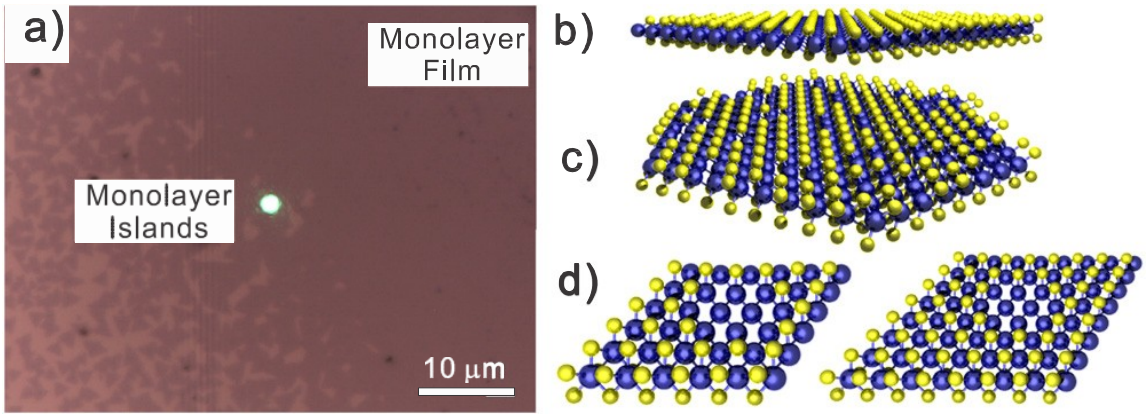

Figure 6.1: (a) Optical micrograph of the type of MoS2 films used in this study, with single-layer islands on the left and a continuous single-layer film on the right of the imaged area. The laser spot is 2 μm in size and was used for measurement of Raman spectra in air. (b) The structure of an ideal MoS_2 monolayer film, consisting of a plane of Mo atoms surrounded by two planes of S atoms. (c) A representation of a possible structure of the film after sputter removal of 12.5% of its sulfur (25% of the top-layer sulfur atoms). (d) A compact 7-atom top-layer sulfur vacancy in the two computational supercells used in this work. These structures were found to be stable within our *ab initio* molecular dynamics simulation at 350 K.

of a MoS_2 film used in this study. Figure 6.1b is a schematic representation of the structure of single-layer MoS_2, which consists of hexagonal top and bottom layers of sulfur surrounding a molybdenum layer. The samples were characterized in air prior to our experiments using Raman and PL spectroscopy. The right portion of the image in Figure 6.1a shows a continuous film of monolayer thickness, while the left area consists of single-layer MoS_2 islands. Both regions exhibit the same PL peak at 1.87 eV, corresponding to the direct band gap. Raman spectra reveal the E_{12g} and A_{1g} modes, with a separation of 21 cm^{-1}, as is typically seen in single-layer MoS2 films prepared by CVD [71, 83].

Once a sufficiently homogeneous area of the MoS_2 film exhibiting exclusively single-layer Raman and PL characteristics had been identified, the sample was attached to a temperature-controlled manipulator in an ultra-high vacuum system. For subsequent studies of sputtering, the system was evacuated and baked to reach a base pressure of 1×10^{-9} Torr. A Varian sputter gun operated at 500 V acceleration potential, 20 mA emission current, and $x \times 10^{-2}$ – 2×10^{-5} Torr partial pressure of Ar was used for generating Ar^+ ions. The sputter beam had a diameter of 0.5 cm. For reference, we measured the sputter current induced by this beam on a copper surface as 0.6 – 2.2 μA, respectively, for the Ar pressures given above. In the following, we will assume this value as an approximation of the beam current.

The XPS measurements were performed using excitation by A1 Kα radiation with the emitted electrons detected by a Scienta R300 hemispheric analyzer equipped with a 2D detector. The PL experiments employed a Spectra Physics Millennia laser operating at a wavelength of 532 nm, a spectrometer with 1200 $frac$linesmm grating blazed at 750 nm, and a liquid-nitrogen cooled Princeton Instruments SPEC-10 CCD detector. For in situ measurements a 50 mm focal length lens inside our UHV system was used to focus $\sim$100 mW of pump beam onto the sample surface with a spot of $\sim$100 μm. This results in an intensity of approximately 10 $\frac{\mu W}{\mu m^2}$, similar to that of typical microscope-based Raman measurements [77]. We collected the resultant PL signal in the back-scattered direction using a dichroic mirror to separate the excitation beam from PL signal.

Vacancy formation energy and thermal stability of the sputtered film was evaluated using the Vienna ab initio simulation package (VASP) [27, 28] to perform density functional theory (DFT) simulations.We employed projectoraugmented wave (PAW) [9,29] and plane-wave basis set methods. We used the PerdewBurkeErnzerhof of functional (PBE) [55] to describe exchange correlation interactions and adopted a cut-off for plane-wave expansion at 500 eV. The conjugate-gradient algorithm [59] was employed for structural relaxation and to optimize lateral atomic coordinates by minimizing the in-plane components of the stress tensor; relaxation was allowed with periodic boundary conditions until all components of the force reached a value below 0:01 $\frac{[eV]}{\text{Å}}$. Given the large number of atoms in the computational supercell (up to 192), we found sampling of the Brillouin zone with one k-point to be adequate for evaluation of the total energy. *Ab initio* molecular dynamic (MD) simulations utilized the Nose algorithm [50] for setting the system temperature and a 3 fs time step. To minimize the computational cost, the cut-off for plan-wave expansion was reduced to 300 eV and the simulations ran for a total time of 12 ps.

6.3 Results and Discussion

Our measurements involved cycles of sputtering at room temperature, in situ acquisition of XPS spectra of the Mo 3d, the S 2p, and the Si 2s levels, as well as in situ PL measurement at variable temperature. To avoid sample degradation, all ex-

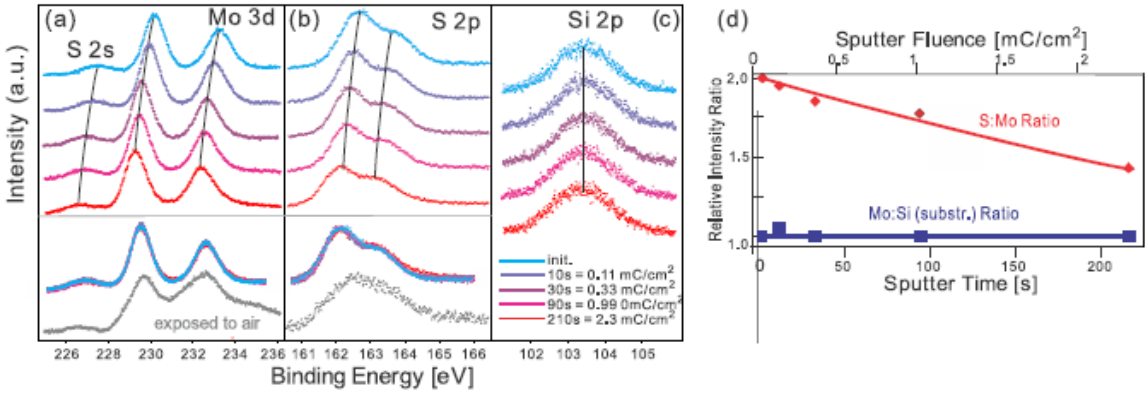

Figure 6.2: XPS spectra of (a) the Mo 3d $\frac{3}{2}$ and $\frac{5}{2}$ states, as well as the S 2s (weak features on the left), (b) the S 2p state, and (c) the Si 2p state. The spectra (from the top to the bottom) were acquired after increasing amounts of sputtering. To account for surface charging, the spectra at different sputter times were aligned so that the Si 2s peak remains at constant energy. The lower parts of (a) and (b) show spectra scaled and shifted for the best overlay of the peak shape, as well as the corresponding spectra after exposure to air. (d) The evolution during sputtering of the intensity of the Mo XPS signal referenced to the substrate Si peak and normalized to unity, and the S:Mo XPS ratio normalized to 2. While the Mo content is seen to remain essentially constant, the amount of sulfur decreases significantly during sputtering.

periments were conducted in immediate succession to one another, with the sample maintained in ultra-high vacuum. Figures 6.2a–c displays the evolution of XPS spectra during sputtering at 2×10^{-5} Torr Ar pressure, corresponding to a net sputter current of 2:2 μA. Figure 6.2a) shows representative spectra of the Mo 3d $\frac{3}{2}$ and $\frac{5}{2}$ peaks for increasing sputter times. The sulfur 2s peak is also visible on the low-energy side of the Mo-derived features. We observe no appreciable reduction in Mo 3d intensity. Further, the shape of the Mo 3d $\frac{3}{2}$ and $\frac{5}{2}$ doublet remains essentially unchanged, as is best seen in the energy-aligned superposition below the individual spectra in Figures 6.2a and b. In order to account for potential charging of the MoS_2 sample on the thick oxide layer, we treat the Si 2p peak Figure 6.2c as a standard and reference

all other states to it. Figure 6.2d shows the evolution of the Mo 3d intensity as a function of sputter time.

The sulfur signal (Figure 6.2b), in contrast to the Mo 3d feature, exhibits a significant reduction in strength from sputtering, with little change of the overall peak shape. Figure 6.2d shows that the total sulfur content, normalized to 2 for the unsputtered film to account for the different XPS yields of the Mo and S states, decreases with sputter time. Within the duration of this experiment, we observe a reduction of the sulfur content of the film by 25%, or 50% of the top sulfur layer in the MoS_2 structure Figure 6.1b. This corresponds to an average sputter yield of 0.03 per Ar^+ ion. A first-order approximation of the sulfur signal decay (red line in Figure 6.2d corresponds to an exponential fit with a rate constant of $1.6 \times 10^{-3} \frac{1}{\mathrm{s}}$ or $1.4 \times 10^{-4} \frac{\mathrm{cm}^2}{\mathrm{C}}$.

We ascribe the selectivity to sulfur removal to the close mass match between the Ar^+ ions and the sulfur atoms, as well as to the low Ar^+ energy; 3 keV Ar^+ ions are capable of removing Mo completely from our substrates. The silicon peak (Figure 6.2c) serves as an internal reference and is not significantly affected by sputtering or exposure to air.

Apart from a shift to lower binding energy, likely arising from charging of the sputtered MoS_2 film with respect to the underlying SiO_2 layer, we observe little change of the peak shape of the Mo^- and S^-derived features (lower part of Figures 6.2a and b). The latter suggests that despite sputtering, the MoS_2 film retains its homogeneity and its overall MoS_2 structure; we speculate that this is achieved by the presence of

an unperturbed bottom sulfur layer that retains the structure of the Mo layer rigid, despite the absence of some of the top-layer sulfur atoms.We further support this argument in the following paragraphs.

Prior to processing, the sulfur and the molybdenum coverage of the samples correlate with one another. There is neither a significant quantity of sulfur in the absence of molybdenum nor is there appreciable incorporation of sulfur into the substrate surface during preparation. We reach these conclusions by aligning the sample so that the spatially resolved axis of our 2D detector lies along the horizontal of Figure 6.1a, i.e., by detecting the XPS yield from sample areas covered by a thick MoS_2 film on one side (where we find strong signal both for S and Mo), across an area with MoS_2 islands (where we find reduced signals for both S and Mo), and ending at a sample area devoid of MoS_2 features on the other side (where we find neither significant Mo nor S signal). This observation indicates that the S/Mo ratio that we track in the XPS-sputter cycles can indeed be related to modification of the MoS_2 monolayer and is not significantly affected by any other possible sulfur source in the surface region. The fact that the MoS2 film is the material being modified is further buttressed by the films dramatic change in stability after processing. XPS measurement on a sputtered film after exposure to air exhibit significantly broadening Mo 3d $\frac{3}{2}$ and $\frac{5}{2}$ peaks, as well as S 2p peaks (bottom of Figures 6.2a and b). We attribute this to extensive oxidation. After sputtering and air exposure, atomic force microscopy reveals degra-

dation in film smoothness, and the films Raman response is significantly reduced. On the other hand, the original, unprocessed films are found to be stable in air.

To confirm that a MoS_2 film with a significant fraction of its top sulfur atoms removed is structurally stable in vacuum for the temperature range of our measurements ($<$350 K), we performed DFT calculations on (6$\times$6) and (8$\times$8) MoS_2 units supercells from which we removed a hexagon of 7 adjacent top-layer sulfur atoms Figure 6.1. Such an arrangement allows us to examine the effect of creation of a relatively large vacancy cluster on the stability of the single-layer MoS_2. Structural relaxation maintains the overall shape of the film and changes the original MoMo bond length inside the S-depleted region $\leq$5%. Allowing the film to evolve at 350 K over a 12 ps interval within ab initio MD leads to no structural change of the film, further supporting the stability of such a sulfur-depleted structure. We note that our calculations do not account for the support of the film structure through an underlying substrate and assume a comparatively large region of depletion of the surface sulfur. Both of these effects generate higher strain than is likely present in the films under experimental conditions.

To explore the impact of sputtering on the optical response of our films, we performed *in situ* PL measurements. Figures 6.3a and b show PL spectra acquired at temperatures of 175 K and 300 K. In both cases, we observe a clear PL signal prior to sputtering, which decays with sputter exposure. The inset of Figures 6.3a and b shows the Mo 3d XPS spectra acquired at 300 K at each of the sputter times, which

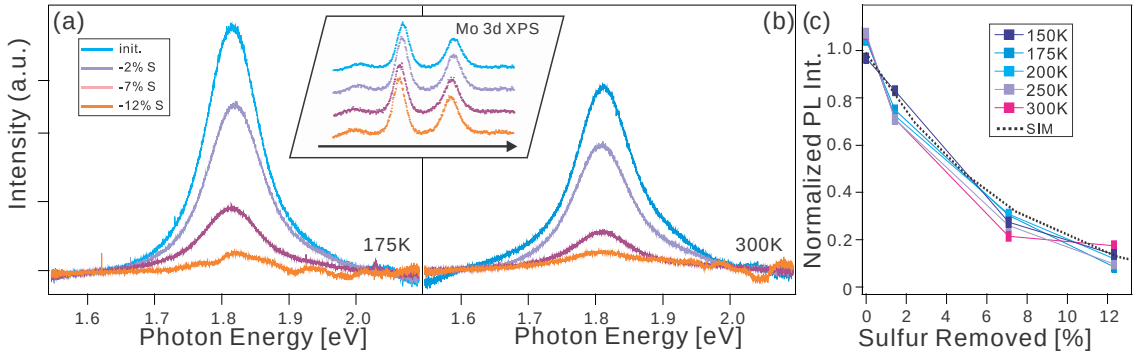

Figure 6.3: PL spectra of a MoS_2 sample for increasing sputter time/sulfur depletion recorded at temperatures of (a) 175 K and (b) 300 K. The inset shows the corresponding Mo 3d $\frac{3}{2}$ and $\frac{5}{2}$ XPS spectra, which remain virtually unchanged. At higher temperatures, a lower initial PL yield is observed; during sputter removal of sulfur the PL yield decreases at both temperatures. (c) The normalized intensity of the PL signal as a function of the percentage of total sulfur removed for different indicated temperatures. The dotted line (sim) corresponds to the model described in the text.

are virtually unchanged throughout the experiment. By comparison of their intensity to the sulfur XPS intensity (not shown), we obtain the amount of sulfur removed. In addition, we observe a well-known reduction of PL yield with increasing temperature [69].

We fitted each PL peak with a Gaussian curve and a constant background. Figure 3(c) shows the evolution of the Gaussian amplitude with sputter time. For purposes of comparison, we plot the relative evolution of the PL yield for each temperature as a function of the reduction in sulfur content of the film (Figure 6.3c.

The PL yield decreases as sulfur is removed. For 10% of sulfur depletion, the PL yield is reduced by almost 80%, i.e., an average decrease of $\sim(7.0 \pm 0.5)\times$ the rate of decrease of the sulfur concentration. Note that in Figure 6.3 and in our discussion the fraction of sulfur is referred to the overall sulfur content of the MoS_2 monolayer

structure. As sputtering is far more likely to remove sulfur in the top layer than in the bottom sulfur layer, the percentage values are twice as high if referred only to the top sulfur layer. As seen in Figure 6.3c, the quenching behavior of the PL is largely unchanged over the temperature regime addressed in this study.

The exciton dynamics underlying the quenching of the PL by sputtering is likely complicated. A rigorous treatment has to account for changes to the MoS_2 band structure, absorbance, and charging, which is beyond the scope of this study. However, we note that good agreement with the data can be achieved if one assumes (a) that the MoS_2 single-layer absorbance is not significantly changed by sputtering, (b) that quenching occurs whenever a photon is absorbed in a MoS_2 unit cell that is perturbed, i.e., missing its top sulfur atom or missing lateral coordination due to a sulfur atom being removed from a directly adjacent unit cell, and (c) that in all other cases the PL yield is identical to the that of the unperturbed system. To obtain values for the PL quenching from these assumptions we have performed a simple simulation (dotted line in Figure 6.3c). Using a MoS_2 film of 200×200 unit cells, we randomly remove a varying fraction of the top-layer sulfur atoms and evaluate for 1000 arbitrarily chosen locations whether or not the unit cell is perturbed (as defined above). While this model provides agreement with the experiment, we note that a combination of less than unity quenching efficiency of defects and longer exciton diffusion lengths would yield similar overall behavior [71].

6.4 Conclusion

In summary, we have shown that sputtering with a beam of low-energy argon ions provides a method for selective desulfurization of monolayer MoS_2. The spectroscopic studies and DFT modeling suggest that the basic physical structure of the MoS_2 remains largely intact as the sulfur is removed. Our findings suggest that low-energy argon sputtering may have significant potential for the activation, functionalization, and modification of MoS_2 layers. Although not studied systematically, the sharp increase in reactivity of the processed MoS_2 monolayer is apparent from its rapid oxidation in air.

Chapter 7

Conclusion

In this thesis two different two dimensional semiconductors were studied. The majority of the work was performed on germanane which little is know about. Molecular beam empitaxy (MBE) growth of $CaGe_2$ was developed as well as a process to convert those films to germanane using a topotactic de-intercalation in HCL. The MBE growth of germanane requires conductive substrates that are opaque near the bandgap making many electrical and optical measurements impossible. A electrochemical delamination process was developed allowing the transfer of germanane to arbitrary substrates roving this hurtle. Absorption and photoluminescence excitation spectroscopy (PLE) indicate a bandgap of 1.9 eV at 5 K. Wavelength dependent photo conductivity (WDPC) shows similar behavior indicating that a band like state is being measured as opposed to localized defects. The large Urbach tail in the absorption, PLE and WDPC indicate the presences of defects showing the material quality has

room for improvement. Time resolved photoluminescence reveal the carrier dynamics.

MoS_2 was also studied. Here a method to create sulfur vacancies by argon sputtering was developed. This allowed us to study the role of defects on photoluminescence (PL). It was seen that a 10% reduction of sulfur leads to a 80% reduction in PL yield. Also the removal of sulfur makes MoS_2 highly reactive allowing for a new method of functionalization.

Bibliography

[1] Patrick; Bushong Elizabeth; O'Hara Dante; Luo Yunqiu; van Baren Jeremiah; Pinchuk Igor; Wu Yi; Ahmed Adam; Katoch Jyoti; Bockrath Marc; Tom Harry; Goldberger Joshua; Kawakami Roland Amamou, Walid; Odenthal. Large area epitaxial germanane for electronic devices.

[2] Maxx Q. Arguilla, Shishi Jiang, Basant Chitara, and Joshua E. Goldberger. Synthesis and stability of two-dimensional ge/sn graphane alloys. *Chemistry of Materials*, 26(24):6941–6946, 2014.

[3] John R. Arthur. Molecular beam epitaxy. *Surface Science*, 500(13):189 – 217, 2002.

[4] C. Ataca and S. Ciraci. Dissociation of h_2o at the vacancies of single-layer mos_2. *Phys. Rev. B*, 85:195410, May 2012.

[5] David D Awschalom, Michael E Flatté, and Nitin Samarth. Spintronics. *Scientific American*, 286(6):66–73, 2002.

[6] MM Benameur, B Radisavljevic, JS Heron, S Sahoo, H Berger, and A Kis. Visibility of dichalcogenide nanolayers. *Nanotechnology*, 22(12):125706, 2011.

[7] F. Besenbacher, M. Brorson, B.S. Clausen, S. Helveg, B. Hinnemann, J. Kibsgaard, J.V. Lauritsen, P.G. Moses, J.K. Nrskov, and H. Topse. Recent stm, {DFT} and haadf-stem studies of sulfide-based hydrotreating catalysts: Insight into mechanistic, structural and particle size effects. *Catalysis Today*, 130(1):86 – 96, 2008. New developments in sulfide catalysis: Linking industrial needs to fundamental challenges Proceedings of the 4th International Symposium on Molecular Aspects of Catalysis by Sulfides (MACS-IV).

[8] Elisabeth Bianco, Sheneve Butler, Shishi Jiang, Oscar D. Restrepo, Wolfgang Windl, and Joshua E. Goldberger. Stability and exfoliation of germanane: A germanium graphane analogue. *ACS Nano*, 7(5):4414–4421, 2013. PMID: 23506286.

[9] P. E. Blöchl. Projector augmented-wave method. *Phys. Rev. B*, 50:17953–17979, Dec 1994.

[10] Ting Cao, Gang Wang, Wenpeng Han, Huiqi Ye, Chuanrui Zhu, Junren Shi, Qian Niu, Pingheng Tan, Enge Wang, Baoli Liu, et al. Valley-selective circular dichroism of monolayer molybdenum disulphide. *Nature communications*, 3:887, 2012.

[11] H. C. Casey, D. D. Sell, and K. W. Wecht. Concentration dependence of the absorption coefficient for n and ptype gaas between 1.3 and 1.6 ev. *Journal of Applied Physics*, 46(1), 1975.

[12] A.Y. Cho and J.R. Arthur. Molecular beam epitaxy. *Progress in Solid State Chemistry*, 10, Part 3(0):157 – 191, 1975.

[13] G., C. Miesner, M.S. Brandt, M. Stutzmann, and G. Abstreiter. Epitaxial alloy films of zintl-phase ca($si_{1-x}ge_x$)$_2$. *Journal of Crystal Growth*, 223(4):573 – 576, 2001.

[14] Libo Gao, Wencai Ren, Huilong Xu, Li Jin, Zhenxing Wang, Teng Ma, Lai-Peng Ma, Zhiyong Zhang, Qiang Fu, Lian-Mao Peng, et al. Repeated growth and bubbling transfer of graphene with millimetre-size single-crystal grains using platinum. *Nature communications*, 3:699, 2012.

[15] Subhamoy Ghatak, Atindra Nath Pal, and Arindam Ghosh. Nature of electronic states in atomically thin mos2 field-effect transistors. *ACS Nano*, 5(10):7707–7712, 2011. PMID: 21902203.

[16] Zoltán Hajnal, Günther Vogg, Lex J.-P. Meyer, Bernadett Szűcs, Martin S. Brandt, and Thomas Frauenheim. Band structure and optical properties of germanium sheet polymers. *Phys. Rev. B*, 64:033311, Jun 2001.

[17] J.J. Harris, B A. Joyce, and P.J. Dobson. Oscillations in the surface structure of sn-doped gaas during growth by {MBE}. *Surface Science*, 103(1):L90 – L96, 1981.

[18] Keliang He, Nardeep Kumar, Liang Zhao, Zefang Wang, Kin Fai Mak, Hui Zhao, and Jie Shan. Tightly bound excitons in monolayer wse_2. *Phys. Rev. Lett.*, 113:026803, Jul 2014.

[19] Marian A Herman and Helmut Sitter. *Molecular beam epitaxy: fundamentals and current status*, volume 7. Springer Science & Business Media, 2012.

[20] M. Houssa, E. Scalise, K. Sankaran, G. Pourtois, V. V. Afanasev, and A. Stesmans. Electronic properties of hydrogenated silicene and germanene. *Applied Physics Letters*, 98(22):–, 2011.

[21] Toshihiro Ichikawa and Shozo Ino. Double diffraction spots in {RHEED} patterns from clean ge(111) and si(001) surfaces. *Surface Science*, 85(2):221 – 243, 1979.

[22] Toshihiro Ichikawa and Shozo Ino. Rheed study on the ge/si(111) and si/ge(111) systems: Reaction of ge with the si(111)(7 7) surface. *Surface Science*, 136(23):267 – 284, 1984.

[23] Shishi Jiang, Sheneve Butler, Elisabeth Bianco, Oscar D Restrepo, Wolfgang Windl, and Joshua E Goldberger. Improving the stability and optical properties of germanane via one-step covalent methyl-termination. *Nature communications*, 5, 2014.

[24] Sajeev John, Costas Soukoulis, Morrel H. Cohen, and E. N. Economou. Theory of electron band tails and the urbach optical-absorption edge. *Phys. Rev. Lett.*, 57:1777–1780, Oct 1986.

[25] Jakob Kibsgaard, Zhebo Chen, Benjamin N Reinecke, and Thomas F Jaramillo. Engineering the surface structure of mos2 to preferentially expose active edge sites for electrocatalysis. *Nature materials*, 11(11):963–969, 2012.

[26] Christian Kisielowski, QuentinM. Ramasse, LarsP. Hansen, Michael Brorson, Anna Carlsson, AlfonsM. Molenbroek, Henrik Topse, and Stig Helveg. Imaging mos2 nanocatalysts with single-atom sensitivity. *Angewandte Chemie International Edition*, 49(15):2708–2710, 2010.

[27] G. Kresse and J. Furthmller. Efficiency of ab-initio total energy calculations for metals and semiconductors using a plane-wave basis set. *Computational Materials Science*, 6(1):15 – 50, 1996.

[28] G. Kresse and J. Hafner. *Ab initio* molecular dynamics for liquid metals. *Phys. Rev. B*, 47:558–561, Jan 1993.

[29] G. Kresse and D. Joubert. From ultrasoft pseudopotentials to the projector augmented-wave method. *Phys. Rev. B*, 59:1758–1775, Jan 1999.

[30] Dattatray J. Late, Bin Liu, H. S. S. Ramakrishna Matte, Vinayak P. Dravid, and C. N. R. Rao. Hysteresis in single-layer mos2 field effect transistors. *ACS Nano*, 6(6):5635–5641, 2012. PMID: 22577885.

[31] Xuesong Li, Weiwei Cai, Jinho An, Seyoung Kim, Junghyo Nah, Dongxing Yang, Richard Piner, Aruna Velamakanni, Inhwa Jung, Emanuel Tutuc, Sanjay K. Banerjee, Luigi Colombo, and Rodney S. Ruoff. Large-area synthesis of high-quality and uniform graphene films on copper foils. *Science*, 324(5932):1312–1314, 2009.

[32] Yanguang Li, Hailiang Wang, Liming Xie, Yongye Liang, Guosong Hong, and Hongjie Dai. Mos2 nanoparticles grown on graphene: An advanced catalyst for the hydrogen evolution reaction. *Journal of the American Chemical Society*, 133(19):7296–7299, 2011. PMID: 21510646.

[33] General Electric Lighting. *Product Catalog*. www.gelighting.com, 06-20-2015.

[34] Jing Liqiang, Qu Yichun, Wang Baiqi, Li Shudan, Jiang Baojiang, Yang Libin, Fu Wei, Fu Honggang, and Sun Jiazhong. Review of photoluminescence performance of nano-sized semiconductor materials and its relationships with photocatalytic activity. *Solar Energy Materials and Solar Cells*, 90(12):1773–1787, 2006.

[35] Han Liu, Adam T. Neal, Zhen Zhu, Zhe Luo, Xianfan Xu, David Tomnek, and Peide D. Ye. Phosphorene: An unexplored 2d semiconductor with a high hole mobility. *ACS Nano*, 8(4):4033–4041, 2014. PMID: 24655084.

[36] Keng-Ku Liu, Wenjing Zhang, Yi-Hsien Lee, Yu-Chuan Lin, Mu-Tung Chang, Ching-Yuan Su, Chia-Seng Chang, Hai Li, Yumeng Shi, Hua Zhang, Chao-Sung Lai, and Lain-Jong Li. Growth of large-area and highly crystalline mos2 thin layers on insulating substrates. *Nano Letters*, 12(3):1538–1544, 2012. PMID: 22369470.

[37] Kain Lu Low, Wen Huang, Yee-Chia Yeo, and Gengchiau Liang. Ballistic transport performance of silicane and germanane transistors. *Electron Devices, IEEE Transactions on*, 61(5):1590–1598, 2014.

[38] Quan Ma, Patrick M Odenthal, John Mann, Duy Le, Chen S Wang, Yeming Zhu, Tianyang Chen, Dezheng Sun, Koichi Yamaguchi, Tai Tran, et al. Controlled argon beam-induced desulfurization of monolayer molybdenum disulfide. *Journal of Physics: Condensed Matter*, 25(25):252201, 2013.

[39] Yandong Ma, Ying Dai, Ying-Bo Lu, and Baibiao Huang. Effective bandgap engineering in wrinkled germanane via tiny electric field. *J. Mater. Chem. C*, 2:1125–1130, 2014.

[40] Kin Fai Mak, Keliang He, Changgu Lee, Gwan Hyoung Lee, James Hone, Tony F Heinz, and Jie Shan. Tightly bound trions in monolayer mos2. *Nature materials*, 12(3):207–211, 2013.

[41] Kin Fai Mak, Keliang He, Jie Shan, and Tony F Heinz. Control of valley polarization in monolayer mos2 by optical helicity. *Nature nanotechnology*, 7(8):494–498, 2012.

[42] Kin Fai Mak, Changgu Lee, James Hone, Jie Shan, and Tony F. Heinz. Atomically thin mos_2: A new direct-gap semiconductor. *Phys. Rev. Lett.*, 105:136805, Sep 2010.

[43] Marina Makarova, Yuji Okawa, and Masakazu Aono. Selective adsorption of thiol molecules at sulfur vacancies on mos2(0001), followed by vacancy repair via sc dissociation. *The Journal of Physical Chemistry C*, 116(42):22411–22416, 2012.

[44] John Mann, Dezheng Sun, Quan Ma, Jen-Ru Chen, Edwin Preciado, Taisuke Ohta, Bogdan Diaconescu, Koichi Yamaguchi, Tai Tran, Michelle Wurch, KatieMarie Magnone, Tony F. Heinz, Gary L. Kellogg, Roland Kawakami, and Ludwig Bartels. Facile growth of monolayer mos2 film areas on sio2. *The European Physical Journal B*, 86(5), 2013.

[45] W Patrick McCray. Mbe deserves a place in the history books. *Nature nanotechnology*, 2(5):259–261, 2007.

[46] K. M. McCreary, K. Pi, and R. K. Kawakami. Metallic and insulating adsorbates on graphene. *Applied Physics Letters*, 98(19):–, 2011.

[47] K. M. McCreary, K. Pi, A. G. Swartz, Wei Han, W. Bao, C. N. Lau, F. Guinea, M. I. Katsnelson, and R. K. Kawakami. Effect of cluster formation on graphene mobility. *Phys. Rev. B*, 81:115453, Mar 2010.

[48] J. F. Morar and M Wittmer. Metallic $casi_2$ epitaxial films on si(111). *Phys. Rev. B*, 37:2618–2621, Feb 1988.

[49] J.H. Neave, B.A. Joyce, P.J. Dobson, and N. Norton. Dynamics of film growth of gaas by mbe from rheed observations. *Applied Physics A*, 31(1):1–8, 1983.

[50] Shuichi Nos. A unified formulation of the constant temperature molecular dynamics methods. *The Journal of Chemical Physics*, 81(1), 1984.

[51] K. S. Novoselov, A. K. Geim, S. V. Morozov, D. Jiang, Y. Zhang, S. V. Dubonos, I. V. Grigorieva, and A. A. Firsov. Electric field effect in atomically thin carbon films. *Science*, 306(5696):666–669, 2004.

[52] A Palenzona, P Manfrinetti, and M.L Fornasini. The phase diagram of the cage system. *Journal of Alloys and Compounds*, 345(12):144 – 147, 2002.

[53] P.W. Palmberg and W.T. Peria. Low energy electron diffraction studies on ge and na-covered ge. *Surface Science*, 6(1):57 – 97, 1967.

[54] Ivan Pelant and Jan Valenta. *Luminescence spectroscopy of semiconductors*. Oxford University Press, 2012.

[55] John P. Perdew, Kieron Burke, and Matthias Ernzerhof. Generalized gradient approximation made simple. *Phys. Rev. Lett.*, 77:3865–3868, Oct 1996.

[56] YU Peter and Manuel Cardona. *Fundamentals of semiconductors: physics and materials properties*. Springer Science & Business Media, 2010.

[57] K. Pi, K. M. McCreary, W. Bao, Wei Han, Y. F. Chiang, Yan Li, S.-W. Tsai, C. N. Lau, and R. K. Kawakami. Electronic doping and scattering by transition metals on graphene. *Phys. Rev. B*, 80:075406, Aug 2009.

[58] Igor V. Pinchuk, Patrick M. Odenthal, Adam S. Ahmed, Walid Amamou, Joshua E. Goldberger, and Roland K. Kawakami. Epitaxial co-deposition growth of cage2 films by molecular beam epitaxy for large area germanane. *Journal of Materials Research*, 29:410–416, 2014.

[59] W.H. Press. *Numerical Recipes 3rd Edition: The Art of Scientific Computing*. Cambridge University Press, 2007.

[60] O. Pulci, P. Gori, M. Marsili, V. Garbuio, R. Del Sole, and F. Bechstedt. Strong excitons in novel two-dimensional crystals: Silicane and germanane. *EPL (Europhysics Letters)*, 98(3):37004, 2012.

[61] Branimir Radisavljevic, Aleksandra Radenovic, Jacopo Brivio, V Giacometti, and A Kis. Single-layer mos2 transistors. *Nature nanotechnology*, 6(3):147–150, 2011.

[62] Michael A Reshchikov and Hadis Morkoc. Luminescence properties of defects in gan. *Journal of applied physics*, 97(6):061301, 2005.

[63] Oscar D Restrepo, Kevin E Krymowski, Joshua Goldberger, and Wolfgang Windl. A first principles method to simulate electron mobilities in 2d materials. *New Journal of Physics*, 16(10):105009, 2014.

[64] Chen Si, Junwei Liu, Yong Xu, Jian Wu, Bing-Lin Gu, and Wenhui Duan. Functionalized germanene as a prototype of large-gap two-dimensional topological insulators. *Phys. Rev. B*, 89:115429, Mar 2014.

[65] Z E. Smith and S. Wagner. Band tails, entropy, and equilibrium defects in hydrogenated amorphous silicon. *Phys. Rev. Lett.*, 59:688–691, Aug 1987.

[66] Andrea Splendiani, Liang Sun, Yuanbo Zhang, Tianshu Li, Jonghwan Kim, Chi-Yung Chim, Giulia Galli, and Feng Wang. Emerging photoluminescence in monolayer mos2. *Nano Letters*, 10(4):1271–1275, 2010. PMID: 20229981.

[67] A. G. Swartz, J. Ciraldo, J. J. I. Wong, Yan Li, Wei Han, Tao Lin, S. Mack, J. Shi, D. D. Awschalom, and R. K. Kawakami. Epitaxial euo thin films on gaas. *Applied Physics Letters*, 97(11):–, 2010.

[68] Adrian Swartz. Investigation of spin-based phenomena in candidate spintronic materials by molecular beam epitaxy. *PhD Thesis University of California Riverside*, 2013.

[69] Sefaattin Tongay, Jian Zhou, Can Ataca, Kelvin Lo, Tyler S. Matthews, Jingbo Li, Jeffrey C. Grossman, and Junqiao Wu. Thermally driven crossover from indirect toward direct bandgap in 2d semiconductors: Mose2 versus mos2. *Nano Letters*, 12(11):5576–5580, 2012. PMID: 23098085.

[70] R. W. Ulbricht, A. Schmehl, T. Heeg, J. Schubert, and D. G. Schlom. Adsorption-controlled growth of euo by molecular-beam epitaxy. *Applied Physics Letters*, 93(10):–, 2008.

[71] Arend M van der Zande, Pinshane Y Huang, Daniel A Chenet, Timothy C Berkelbach, YuMeng You, Gwan-Hyoung Lee, Tony F Heinz, David R Reichman, David A Muller, and James C Hone. Grains and grain boundaries in highly crystalline monolayer molybdenum disulphide. *Nature materials*, 12(6):554–561, 2013.

[72] YP Varshni. Temperature dependence of the energy gap in semiconductors. *Physica*, 34(1):149–154, 1967.

[73] G. Vogg, M. S. Brandt, and M. Stutzmann. Polygermynea prototype system for layered germanium polymers. *Advanced Materials*, 12(17):1278–1281, 2000.

[74] G. Vogg, M.S. Brandt, M. Stutzmann, I. Genchev, A. Bergmaier, L. Grgens, and G. Dollinger. Epitaxial cage2 films on germanium. *Journal of Crystal Growth*, 212(12):148 – 154, 2000.

[75] Günther Vogg, Lex J.P. Meyer, Christian Miesner, Martin S. Brandt, and Martin Stutzmann. Polygermanosilyne calcium hydroxide intercalation compounds formed by topotactic transformation of ca($si_{1x}ge_x$)$_2$ alloy *Zintl* phases in ambient atmosphere. *Monatshefte für Chemie / Chemical Monthly*, 132(10):1125–1135, 2001.

[76] Michael Wahl. Time-correlated single photon counting. *Technical Note. PicoQuant GmbH*, 2014.

[77] Qing Hua Wang, Kourosh Kalantar-Zadeh, Andras Kis, Jonathan N Coleman, and Michael S Strano. Electronics and optoelectronics of two-dimensional transition metal dichalcogenides. *Nature nanotechnology*, 7(11):699–712, 2012.

[78] Yu Wang, Yi Zheng, Xiangfan Xu, Emilie Dubuisson, Qiaoliang Bao, Jiong Lu, and Kian Ping Loh. Electrochemical delamination of cvd-grown graphene film: Toward the recyclable use of copper catalyst. *ACS Nano*, 5(12):9927–9933, 2011. PMID: 22034835.

[79] Jared Wong. Controlling magnetism at the nanoscale. *PhD Thesis University of California Riverside*, 2012.

[80] Di Xiao, Gui-Bin Liu, Wanxiang Feng, Xiaodong Xu, and Wang Yao. Coupled spin and valley physics in monolayers of mos_2 and other group-vi dichalcogenides. *Phys. Rev. Lett.*, 108:196802, May 2012.

[81] Yong Xu, Binghai Yan, Hai-Jun Zhang, Jing Wang, Gang Xu, Peizhe Tang, Wenhui Duan, and Shou-Cheng Zhang. Large-gap quantum spin hall insulators in tin films. *Phys. Rev. Lett.*, 111:136804, Sep 2013.

[82] Hualing Zeng, Junfeng Dai, Wang Yao, Di Xiao, and Xiaodong Cui. Valley polarization in mos2 monolayers by optical pumping. *Nature nanotechnology*, 7(8):490–493, 2012.

[83] Yongjie Zhan, Zheng Liu, Sina Najmaei, Pulickel M. Ajayan, and Jun Lou. Large-area vapor-phase growth and characterization of mos2 atomic layers on a sio2 substrate. *Small*, 8(7):966–971, 2012.

[84] Guanhua Zhang, Huajun Qin, Jing Teng, Jiandong Guo, Qinlin Guo, Xi Dai, Zhong Fang, and Kehui Wu. Quintuple-layer epitaxy of thin films of topological insulator bi2se3. *Applied Physics Letters*, 95(5):–, 2009.

[85] Yijin Zhang, Jianting Ye, Yusuke Matsuhashi, and Yoshihiro Iwasa. Ambipolar mos2 thin flake transistors. *Nano Letters*, 12(3):1136–1140, 2012. PMID: 22276648.

[86] Yuanbo Zhang, Yan-Wen Tan, Horst L Stormer, and Philip Kim. Experimental observation of the quantum hall effect and berry's phase in graphene. *Nature*, 438(7065):201–204, 2005.

[87] Z. Y. Zhu, Y. C. Cheng, and U. Schwingenschlögl. Giant spin-orbit-induced spin splitting in two-dimensional transition-metal dichalcogenide semiconductors. *Phys. Rev. B*, 84:153402, Oct 2011.

[88] Horst Zimmermann and H Zimmermann. *Integrated silicon optoelectronics*. Springer, 2010.

Appendix A

Optics Tricks

A.1 Introduction

Throughout this thesis fiber optics, white light sources and spectrometers/monochromators were extensively used. While the naive can use these with reasonable success, there are many tricks that I learned in my time with the Crooker lab that I will relay here.

A.2 F-number and Numerical Aperture

Two of the most useful numbers that describe how optical systems gather light are F-number(F#) and numerical aperture(NA). F# is defined at the ration of the focal length and the diameter of the optic (equation A.1).

$$F\# = \frac{f}{D} \tag{A.1}$$

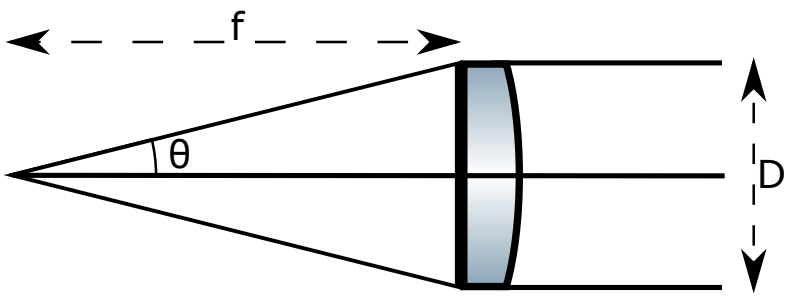

Figure A.1: Diagram of a lens showing the relations for F# and NA

This is a basic number that describes the maximum cone of light that an optic can collect from a point source located at the focal point or the cone produced by focusing a collimated beam that fills the optic. More commonly found on optics specifications is NA. NA is defined as

$$\text{NA} = n\ Sin\left(\theta\right) \tag{A.2}$$

where *n* is the index of refraction and θ is the half angle of the maximum cone of light that an optic can collect (see Figure B.4 for details). For optics in air $n = 1$ and NA simplifies to $NA = Sin\left(\theta\right)$. As NA is not easy to measure, thankfully there is a easy

conversion between the two if you are in the small angle limit ans is derived below.

$$\begin{aligned} NA &= Sin\,(\theta) \\ &\approx Tan\,(\theta) \\ &\approx \frac{\mathrm{D}}{2f} \\ &\approx \frac{1}{2\mathrm{F}\#} \end{aligned} \tag{A.3}$$

A.3 White light sources

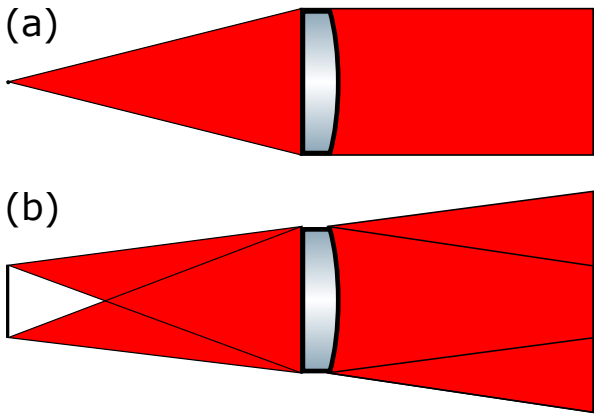

Figure A.2: (a) Diagram of a collimated point source (b) Diagram representing why a non point source cannot be collimated.

White light was used extensively in this thesis and it came from a verity of sources. The simplest source used was a standard incandescent 60 W light bulb. It's spectrum is modeled well by a 2800 K [33] blackbody. While this is the simplest source it is not a very good option if you need to collimate the light as the filament is very long. Light from different parts of the filament will strike the lens at different angles translating

into collimated beams going different directions (Figure A.2b) making it impossible to collimate. The solution is to use a point source. In general, xenon arc-lamps are very close to being point sources and usually can be well collimated. The EQ-99X from Energetiq is a laser assisted xenon lamp that has an especially small spot and works well for producing collimated white light. If a point source is not available and collimated white light is needed, a point source can be created by focusing white light through a single mode fiber and then collimating the output. While this works, it has high loss and may not be the best solution if high power is needed.

A.4 Dealing with fiber optics

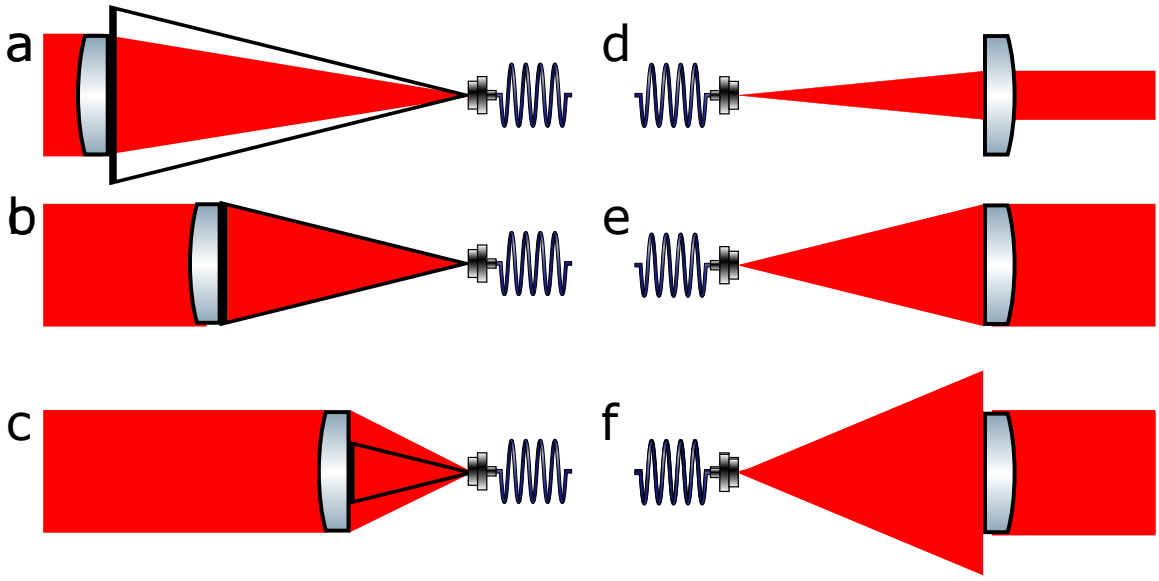

Figure A.3: Diagram showing coupling into a fiber optic for the (a) under filled (b) NA matched and (c) overfilled cases. The black triangle represents the acceptance cone of the fiber. Diagram of light collimation from a fiber for the (e) under filled (f) NA matched and (g) overfilled cases

Often times it is convenient to transport light from one place to another using fiber optics. There are a few tricks to for optimum coupling. A fiber optic has an acceptance cone where all light coming from this cone is totally internally reflected and thus propagates down the fiber and light outside this cone does not. To get the most light into the fiber one must match the NA of the fiber and the NA of the focusing lens or mirror. If you use a focusing lens with too large a NA the fiber is consisted overfilled and light leaks out of the sides of the fiber Figure (A.3d). If the NA is too small the fiber is under filled concentrating the light into fewer modes and increasing loss (Figure A.3c). With these two options it is generally better to err on the under filled side. Another consideration to couple into a fiber is spot size verse fiber core size. Again, the best results are when the sizes match. For small fibers, aspheric lenses and microscope objectives are useful. Also if you are using white light, achromatic optics are necessary.

Collimating light out of a fiber optics is similar but opposite to focusing light into a fiber. Light coming out of a fiber will be in a cone that is described by the NA. Best results occur when you match the NA. If the lens NA is too small, some of the light coming out of the fiber is not collected (Figure A.3f). If the NA is to large you only use part of the lens decreasing efficiency (Figure A.3d). Though using a lens with too large of a NA can be a simple way reduce the size of the resulting beam. A better option would be to use a lens of the correct NA but small focal length. As the

fiber core gets larger, it will become increasingly harder to collimate the beam as the source is not a point (Figure A.2b).

A.5 Coupling into a spectrometer

Before one can properly couple into a spectrometer, it is necessary to understand how it operates. Here, I will describe the operation of a Czerny-Turner spectrometer. Light passes through an external slit and collimated by a curved mirror and is reflected towards a diffraction grating. The diffraction reflects the light towards another curved with different colors going at slightly different angles. The second curved mirror focuses the light onto a sensor with the different angles of light transforming to different positions giving spectral resolution. A diagram of how this works is seen is Figure A.4. It is important to note the resolution of the spectrometer can be severely affected if the slit is too large. A too large slit will not allow the first curved mirror to collimate the light giving rise to angular separation that is not caused by the diffraction grating.

Since the entrance slit needs to remain small to maintain high resolution it can be beneficial to focus the incoming light into the spectrometer to increase throughput. If the light is directly coupled into the spectrometer, one only has to match the NA of the spectrometer. The NA is set by the focal length and diameter of first curved mirror.

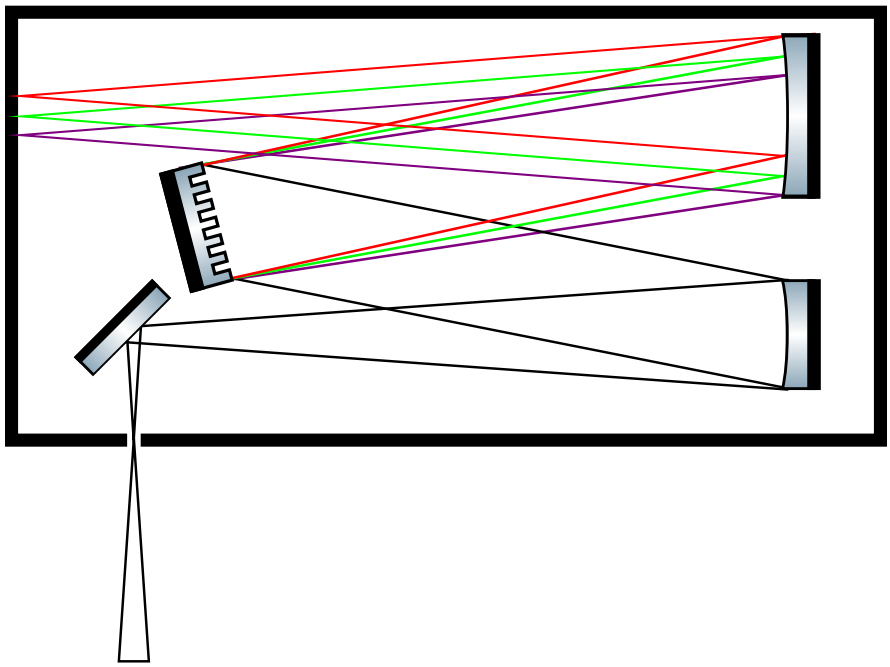

Figure A.4: Diagram showing a Czerny-Turner spectrometer works

It is often convenient to couple the spectrometer to the experiment using a fiber optic. It is rare that a fiber optic has the same NA at the spectrometer. One can use different lenses to match the NA of spectrometer and fiber separately. This removes losses from the NA mismatch but it also will have the affect of magnifying the spot size at the slit increasing the amount of loss at the slit. If you enforce a magnification of 1, both lenses the same, you will get loss from not matching the NA of fiber, spectrometer or both. Experimentally is seems to be a wash to what technique gives maximum signal. The most important is to minimize other losses such as imperfect alignment.

A.6 Correcting a photoluminescence spectrum using white light

The senors in a spectrometer can often give rise to artifacts, such as spectral response and etalon modes that need to be corrected for. This can be done using a white light. First, you must collect a white light and a dark spectrum in the same region as your signal. For the case of etalon modes this spectrum must be taken on the same place on your sensor as your signal as the etalon modes of the sensor are position dependent. Second, you subtract the dark spectrum from your signal (Figure A.5b). Third, you divide that resulting spectrum by the white light spectrum (Figure A.5c). If the white light spectrum in not flat in the region you are correcting for you must also correct for the shape of the white light. The spectrum of 60 W tungsten light bulb is fairly flat in the visible region and does not normally require correction but one can the light as a black body to remove any shape change.

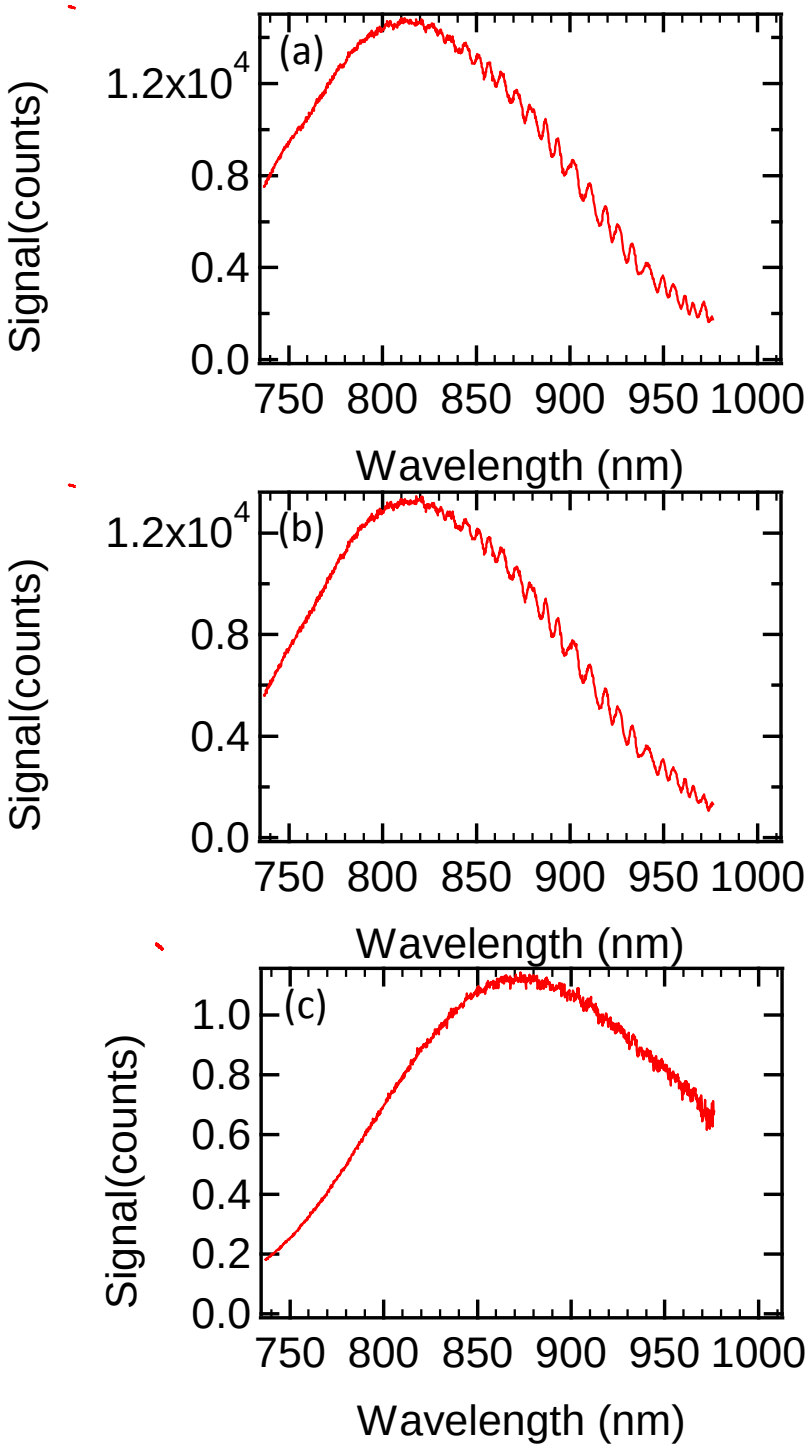

Figure A.5: (a) Uncorrected germanane PL spectrum showing etalon modes. (b) Germanane PL spectrum after dark spectrum subtraction. (c) Final corrected germanane PL

Appendix B

Photoluminescence Alignment

B.1 Introduction

B.1.1 Setup

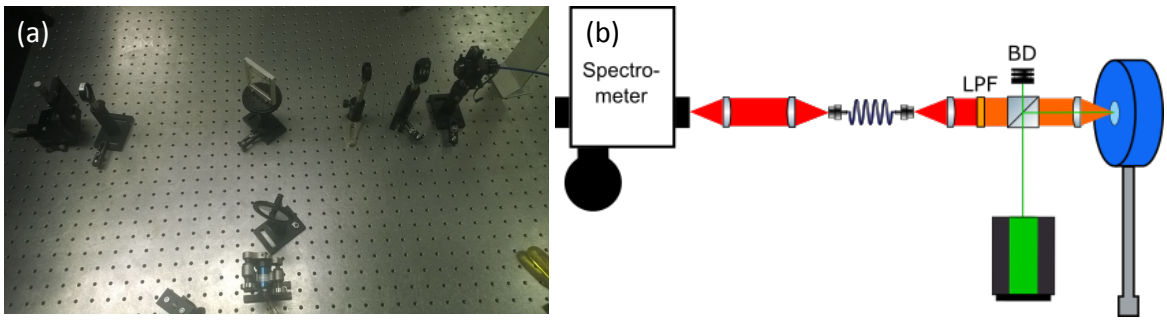

Figure B.1: (a) picture of an actual PL setup. Note the spacing seen in this picture is large to keep from bumping optics during alignment. It can be made much smaller if space dictates. (b) diagram of the PL setup in (a)

In this section I will describe the setup procedure and for one of the photoluminescence setups in described in Chapter 2 and seen in Figure B.1. This is the simplest setup described and is also the one used most often in this thesis.

B.2 Setup

B.2.1 Light source and sample holder selection

The first things you must do are choose your light source and sample holder. The sample holder should be mount placed on an XYZ stage. If you need vacuum or low temperatur, a cryostat should be used. If not, a simple plate bolted to a stage works. An XYZ stage is very useful for a PL measurement. It lets you scan around the sample and adjust focus without moving any optics.

Your light source doesn't need to be fancy. I have used laser pointers before. You need a collimated monochromatic light source with photon energy above the bandgap energy of your sample. A laser is a very nice option but an arc-lamp can work. Your light source does not need to be very powerful. I rarely use more then a few hundred microwatts. Most it important is a stable intensity and a clean spectrum (no extra lines that are not from the fundamental color). It is possible to clean up the spectrum with a filter but if this can be avoided it makes life simpler. Another consideration is laser mount. A mount that has adjustable height and can be leveled is nice though

mirrors can be used if this is not an option. Dragon lasers 532 nm M series laser is a good option for a light source.

B.2.2 Laser

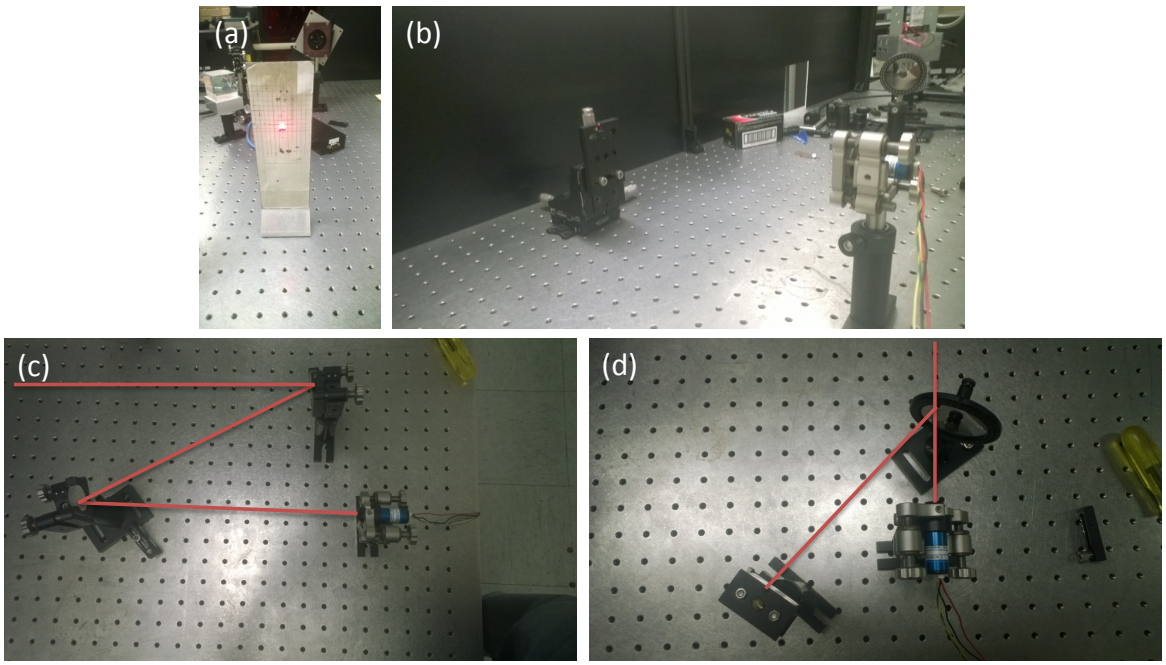

Figure B.2: (a) picture of the alignment tool. (b) setting the height of an adjustable laser. (c) the Z mirror setup for leveling a fixed laser. (d) a final laser setup for PL

You will need to make you laser beam parallel to the table top and at the same height as your sample. There are two cases of lasers that I will explain here. First, the case were the laser's height and tilt can be adjusted and second, the case where the laser is fixed. For the adjustable laser you first need to level the laser beam. The way to check this is to take you alignment tool (grid paper glues to an upright stand as seen in Figure B.2a) and check the height of the laser beam close to the laser and

a few feet away. Adjust the tilt of the laser until the heights are the same. Next you need to adjust the height of the laser such that it hits the center of your sample on the sample holder (Figure B.2b).

For the fixed laser case, you will have to set up two mirrors in a Z shape after the laser (Figure B.2c). To align this, set the height of the second such that the center of the mirror is at the same height as the center of your sample. Then use the first mirror to direct the laser beam to the center of the second mirror. Then level the beam using the second mirror and the alignment tool. If done correctly you will be close to the correct height of the sample. Walk the laser between the two mirrors to get the correct height. Make sure the beam is level once you are at the correct height.

Once the laser is leveled and at the correct height, place the or adjust the second mirror such that the laser beam is parallel to the hole on the optics table. This is not strictly but will make the rest of the alignment much easier. To do this, again use the alignment tool. This time place the alignment tool near the laser such that one side of the base is on the edge of the holes in the optics table and record the position of the laser beam. Repeat this with the same row of holes several feet away from the laser. Make adjustments until the laser hits in the same place at both locations.

To finish the laser setup add laser line filters and and OD filters as needed need to clean up the spectrum and change intensity. I find a graded filter wheel is nice to give better control over laser intensity. When adding filter be very careful to block the

reflected beams as these are an eye hazard. The finished laser setup is seen in Figure B.2d.

B.2.3 Beam splitter and sample holder

Next you will need to setup the beam splitter and sample holder. You have a couple options for a beam splitter. You can use a cube beam splitter, a plate beam splitter or a dichroic mirror. A dichroic mirror is the best option as you will lose less signal when the PL is reflected back through it. Often, you will not have the correct dichroic mirror leave beam splitters as your only option. I prefer plate beam splitters as they give you less reflected beams then cube beam splitters. Also when you selected a beam splitter it must be large enough not to block the collimated PL coming off of the sample.

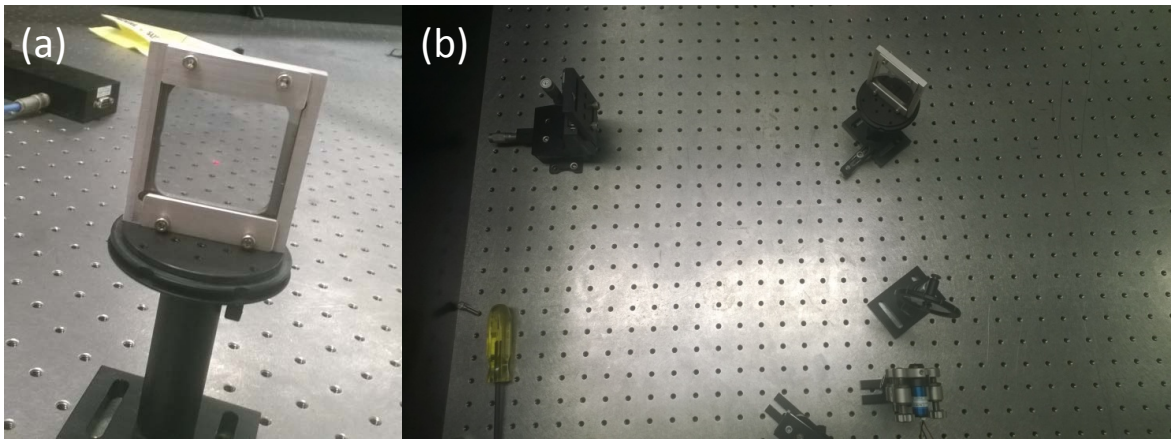

Figure B.3: (a) picture of the laser spots overlapping in the beam splitter (b) Setup after installation the beam splitter and sample holder

Place the beam splitter that you select a couple of inches away from your laser with the laser beam hitting the center of the optic. Exact distance does not matter. It is determined more by space constants then by physics. Rotate the beam splitter such that the reflected beam is 90° from the indecent beam. If you aligned the laser to the table holes you can check this using the alignment tool and aligning the laser with a row of holes that are perpendicular to the original row. Put a beam block on the transmitted beam to prevent eye hazards. Place the sample holder several inches away from the beam splitter along the plat of the reflected beam. Adjust your sample holder so the beam is in the center of your sample and rotate it so the beam reflected off the sample hits the beam splitter in the same part as the incident laser as seen in Figure B.3a. This will keep the laser beam along the path of the holes for easier alignment. The setup at the end of this step is seen in Figure B.3b.

B.2.4 Focus and collection lens

In this setup the same lens is used to focus the laser beam and collect the PL. You can use a lens or a microscope objective. Microscope objectives typically have higher collection efficiency then lens and will have a smaller spot size leading to higher excitation density. A lens many times has a longer focal length giving more room for a cryostat. For most cases where you don't need a small spot a lens will work fine. If you choose a lens you will want to choose a lens with a large numerical aperture (NA) to get the best collection efficiency. The ways to maximize NA is to make the

focal length smaller and make the diameter bigger. The focal length is limited by your cryostat. For very short focal lengths you will need to use an aspherical lens to prevent abortions. The diameter is limited again by space and lenses available. Also every optic after the collection lens will have to be the same size or larger to prevent them form blocking the PL. I generally find a 50mm 1 inch diameter lens works well.

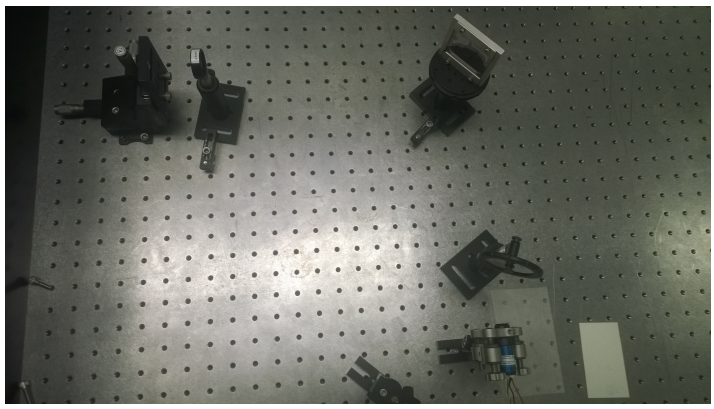

Figure B.4: placement of the focus and collection lens

There is a trick to make placing the focus and collection lens much easier. You should place the alignment such that you see the beam reflected off the sample after it goes though the beam splitter and note the location of the beam. Place the focus and collection lens perpendicular to the beam with the sample at the focal point as seen in Figure B.4. Adjust the lens so that the beam on the alignment tool hits the same spot and is the same size as before. This will get the sample close to the focal point and the laser through the lens center. If your sample stage doesn't have Z motion (focusing) it is convenient to put this lens on a stage to allow focusing.

B.2.5 Coupling to a spectrometer

You can either direct couple to a spectrometer or fiber couple to a spectrometer. Fiber coupling allows for more flexibility in placement and easier data correction. Direct coupling is easier and has a higher signal throughput. I found fiber coupling more useful and will describe it here. Fiber selection will be specific to the wavelength range but in general mulitmode fibers work well. To fiber couple place the fiber optic in a fiber chuck perpendicular to the beam reflected of the sample such that the laser hits the core of the fiber (Figure B.5a). Focus the laser into the fiber using a NA matched lens as seen in Figure B.5b (see Appendix A for discussion).

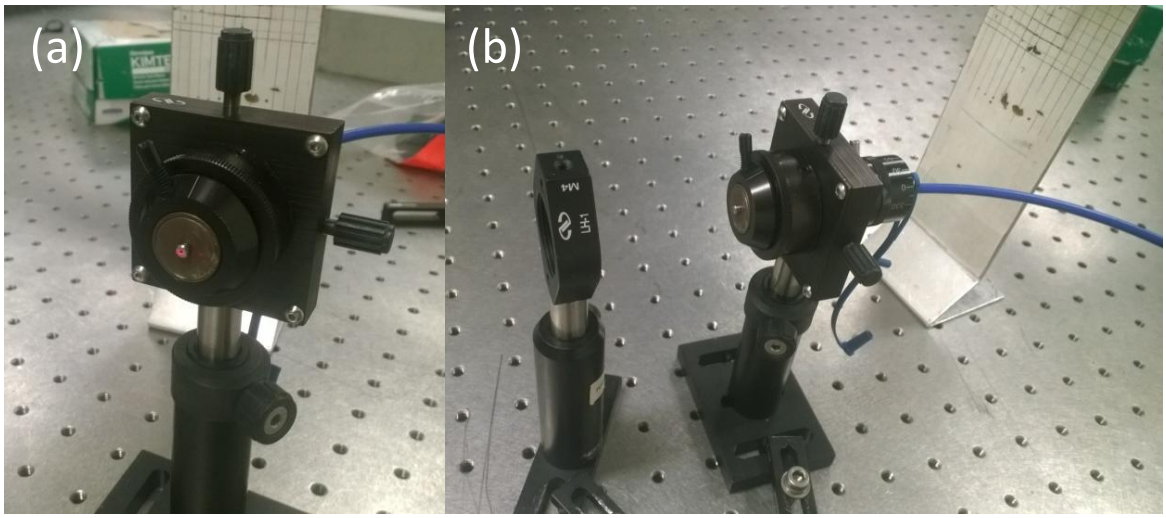

Figure B.5: (a) fiber chuck with the unfocused laser going into the fiber. (b) light focused correctly into the fiber.

Before aligning the fiber to the spectrometer, you need to make sure that you can't shine the laser onto the camera. In the Acton spectrometer this is as simple as selecting the auxiliary port. In others you can just close the slit. Place the fiber in a

fiber chuck about 6-12 inches from the spectrometer such that the laser light forms a circle centered around the slit of the spectrometer. Use a lens to collimate the light from the fiber keeping the collimated light centered around the slit. Then use another lens to focus the light into the spectrometer. A discussion on what lenses to use and other considerations when coupling to a spectrometer is given in Appendix A. Finally place a long pass filter that will block the laser before the optics that couple into the fiber. Make sure the filter is aligned so it doesn't block the PL. The finished setup is seen in Figure B.1a.

B.3 Optimizing signal

To get signal in a new setup you should use a sample that has known large PL like GaAs or ZnSe quantum dots. If you did everything right you should immediately be able to get signal. If you do not have signal please go to the next section on troubleshooting. Once you have signal you will need to maximize it. All of the lens were setup using the excitation laser and there focus will be off for the PL. First, setup the spectrometer to continuously take data. Then adjust the focus of the sample until the signal is maximized. Having a Z stage here makes this easy. Then move to the first fiber chuck adjust the X Y and Z controls to maximize the signal. You may have to go back and forth between the controls to get the maximum. Finally, repeat this

procedure on the second fiber chuck. You are now setup. If you change samples it is a good idea to re-maximize the signal.

B.3.1 Troubleshooting

There are several things to check if you have no signal. First, you should check and make sure the slits on the spectrometer are open], that the spectrometer is setup correctly (light going to the detector ect.) and that you are hitting the sample. If that is fine, block light from getting to the camera and remove the long pass filter. Then check to make sure the laser light is going into the slit. If you still don't have signal, drop the laser power to a safe level for the detector and see if you can see the laser in the signal. If you do follow the maximization procedure and see if you then have signal. If you still do not get signal find a sample that you can see the PL by eye (eg. ZnSe quantum dots) and realign the optics after the sample using the PL light.

Appendix C

Scanning Laser Microscope

C.1 Introduction

Over the course of my thesis work I built several tools to do various experiments. One of the most useful, was a scanning laser microscope. Many times the samples that we have access to are quite small which require the optical setups to use of a high power microscope objective. Normally, aligning the objective to the sample is accomplished by moving the sample. This works fine if the sample is mounted in something light but we found moving the Janis ST-100 crystal caused a lot of vibrations. The alternative is to move the microscope object which is much lighter. Also since it is much lighter the objective can be easily moved by a motorized actuator allowing for scanning. Moving the microscope objective does cause complications as you are now changing the optical path as the objective moves. Dr. Kawakami and

I designed a scanning optical laser microscope that overcomes this challenge. The design and testing of the microscope are given bellow.

C.2 Design

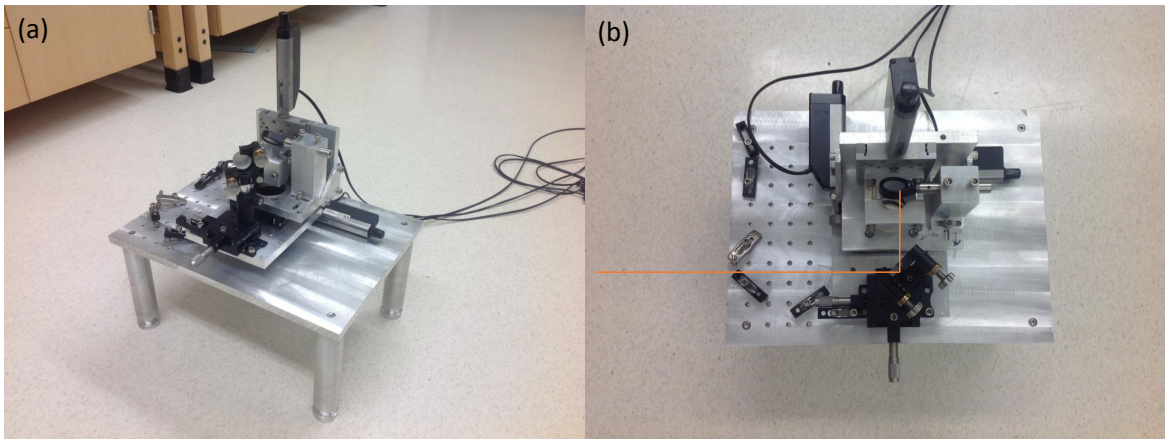

Figure C.1: (a) Image of the Scanning Laser Microscope (b) beam path of the Scanning Laser Microscope

The scanning laser microscope is a stack of linear motion stages that move in line with the laser beam. The bottom stage (typically the x motion) move in the direction of the incident laser beam and holds a mirror that reflects the laser 90° to be along the next axis. The second stage (typically the y stage) is attached on top of the bottom stage but is rotated 90°. It holds a mirror that directs the laser beam straight down as well as the top stage. The top stage holds the microscope objective and allows for focusing. Since the beam path is in line with the line of motion there, the beam hits the same spot on each of the mirrors and focuses through the same spot of the objective. A picture depicting the beam path is given in Figure C.1b.

There are a couple unique design elements in the scanning laser microscope. First, we chose motion stages that have a large central hole. This allows the microscope objective to be centered on the stage instead of hanging off to one side improving stability. Secondly, the mirrors have XY motion to facilitate alignment. Since the laser beam has to be aligned to motion stage to maintain alignment, the typical mirror tilt controls can't be used to adjust the position of the beam. The position is instead changed by translating the mirror. The first mirror is translated by and XY stage which works quite well. Due to space limitations the second mirror translation is done by slotted bolt holes. This doesn't allow for fine motion and should be upgraded in any future versions of the stage.

C.3 Alignment Instructions

The alignment of the Scanning laser microscope is straightforward. You align it stage by stage and with care you can get good results. The process is similar to aligning a delay stage (often found in the Kawakami Lab in a time resolved Kerr rotation setup) but easier as the distance of travel is much shorter. This alignment procedure assumes you have already set the incident laser beam to the correct height and is parallel to the table.

C.3.1 Aligning the first stage

To align the first stage you must rotate the entire microscope such that the incident laser beam is parallel to the motion and strikes the center of the first mirror. Once you get the first stage aligned by eye, I find it easiest to clamp down one of the legs to use as a pivot point. You then put a piece of graph paper in front of the first mirror and run the stage back and forth the full motion. Keep adjusting the rotation until the laser spot does not move on the graph paper. Once it is aligned clamp down all the legs.

C.3.2 Aligning the second stage

Rotate the first mirror such that the beam is roughly parallel to the motion of the second stage and lock it down so it can't move. Place the graph paper before the second mirror and run the second stage back and forth the full motion adjusting the first mirrors tilt controls until the laser spot is steady on the graph paper.

C.3.3 Aligning the third stage

The alignment of the third stage is the hardest but ultimately matters the least as the focus is not usually changed during a scan. For this stage I use the quality of the reflected beam as the judgment criteria for good alignment. If you are aligned

through the center of the microscope objective and go reasonable straight through it the beam will defocus into a nice circle on both sides of the focal point.

To start the alignment place a beam splitter before the scanning laser microscope such that the reflected beam will be split out. Also place something reflective at the focus of the objective. A piece of SiO_2/Si works well for visible and NIR. Then align the beam over the top of the objective using the XY translation on the first mirror. Next position the second mirror so that the beam go straight through the center of the objective. Adjust the XY translation of the first mirror and the position of the second mirror until the reflected beam is circular on both sides of the focal point. Once that is achieved bolt everything down tightly.

On certain setups it is advantages for the laser beam to not go through the center of the objective so that the reflected beam with come back separated from the indecent beam. To achieve this, align everything as normal and then use the XY stage on the first mirror to translate the laser beam of center of the objective.

C.4 Characterization of Performance

Before the Scanning Laser Microscope could be used for experiment it had to be tested. Scanning reflectivity was used to test the scanning ability as well as to characterized the spot size. Scanning reflectivity was performed by aligning a HeNe laser through the Scanning Laser Microscope and measuring the intensity of the reflected

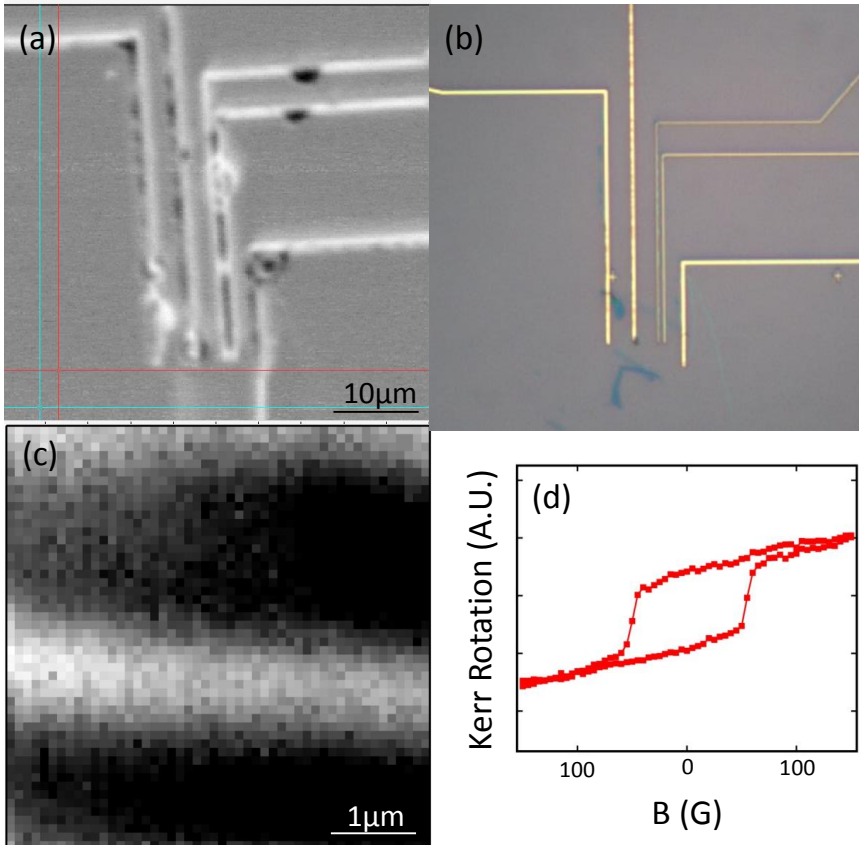

Figure C.2: (a) Scanning reflectivity image of a graphene spin valve with 200 nm step size. (b) Corresponding optical micro-graph of the graphene spin valve in a. (c) Scanning reflectivity image of a gold wire showing the resolution of the Scanning laser Microscope with 100 nm step size. (d) MOKE loop of iron taken through the Scanning Laser Microscope

beam that was picked off using a beam splitter. A chopper and lock-in were used so that the experiment could be done with the room lights on. A graphene spin valve in air was used as a test sample for the scanning. As seen in Figure C.2 a and b the reflectivity image matches the optical image without distortions demonstrating the scanning ability of the microscope. The spot size was determined by scanning the edge of one of the gold contacts. The blurring of the sharp edge will give an idea of the laser spot size. Figure C.2 c shows a blurring of about 700 nm. This is larger then

the diffraction limit of 575 nm which might be due to the 100 nm resolution of the stepper motors. Features less than 700 nm can been seen but they will not be well resolved. This can be seen in the blurring of the two electrodes in Figure C.2 a. It is to be noted that the resolution will be degraded if the experiment is performed in a cryostat as the laser must bas through a window.

To determine the suitability for Kerr rotation experiments, magneto optical Kerr Effect (MOKE) was performed on a thin film of iron placed in a cryostat. A description of MOKE can be found in reference [79]. Figure C.2 d shows the resulting MOKE loop demonstrating the Scanning Laser Microscopes ability to perform Kerr rotation experiments.